Chemical Geology 519 (2019) 95–109

Contents lists available at ScienceDirect

Chemical Geology

journal homepage: www.elsevier.com/locate/chemgeo

Diagenesis and iron paleo-redox proxies: New perspectives from magnetic and iron speciation analyses in the Santa Barbara Basin

Yi Wang[a,*], Ingrid L. Hendy[a], Jennifer C. Latimer[b], Dario Bilardello[c]

[a] Department of Earth and Environmental Sciences, University of Michigan, Ann Arbor, MI 48105, USA
[b] Department of Earth and Environmental Systems, Indiana State University, Terre Haute, IN 47809, USA
[c] Institute for Rock Magnetism, University of Minnesota, Minneapolis, MN 55455, USA

ARTICLE INFO

Editor: Michael E. Böttcher

Keywords:
Diagenesis
Iron speciation
Trace metals
Magnetism
Santa Barbara Basin

ABSTRACT

Sedimentary redox proxies are usually employed to reconstruct the paleo-redox conditions of bottom water environments, assuming that porewater and bottom water dissolved oxygen concentrations are similar. Using a combination of geochemical and magnetic techniques, we investigate the relationship between iron speciation and mineralogy in recent (~1760–2009 CE) sediments retrieved from the Santa Barbara Basin (SBB) – a modern silled basin with low-oxygen (dissolved O_2 < 10 μmol/kg) and sporadically anoxic (no O_2 detected) bottom waters. Magnetic analyses reveal that biogenic magnetite is preserved in SBB sulfidic porewaters on at least decadal to centennial time scales. Highly-reactive Fe (oxyhydr)oxides remain preserved despite observed sulfidic porewaters, indicating incomplete pyrite conversion, and producing low Fe_{py} [pyrite Fe]/Fe_{HR} ratios. We attribute this observation to restricted porewater reaction kinetics under high sedimentation rates. Our results also reveal non-steady state diagenesis caused by instantaneous depositional events (e.g., turbidites and flood layers). The most reducing water column suggested by Fe speciation coincided with the *Macoma* layer, where in situ colonization of hypoxia-intolerant bivalve shells argues for the most oxygenated bottom water in the 250 year record. A turbidite potentially introduced fresh unsulfidized Fe_{HR} that buffered upward-diffusing sulfide from underlying sediments. Subsequent pyrite precipitation following re-establishment of sulfidic porewaters could have facilitated a "false positive" interpretation. In comparison, redox-sensitive metal enrichments (Mo_{EF}, U_{EF}, and Re_{EF}) were not obscured by post-depositional diagenesis and appear to accurately record redox geochemistry at the sediment-water interface.

1. Introduction

Redox environments are central to both paleo- and modern oceanographic studies due to their relationship with atmospheric and/or oceanic oxygenation through geologic time. However, the limited timespan (several decades) of dissolved oxygen (DO) instrumental records in the oceans is insufficient to identify the potential extremes or full magnitude of DO change. To reconstruct past DO changes in the ocean, numerous approaches have been applied, of which sedimentary geochemical proxies (e.g., redox-sensitive metal enrichments, isotopes and speciation) are the most widely used. Geochemistry of these proxies depends directly on the ambient anoxic (no O_2 detected)/euxinic (sulfide-rich anoxic) conditions under which they were generated and then preserved. Iron speciation techniques in particular (Poulton and Canfield, 2005) have been widely used on sedimentary rocks as a redox proxy that can distinguish oxic, ferruginous (iron-rich anoxic water column), and euxinic water columns on different time scales (Cheng et al., 2016; Li et al., 2010; Li et al., 2015; Lyons et al., 2014; Lyons and Severmann, 2006; Reinhard et al., 2009; Tessin et al., 2016).

Extensive calibration on modern surface marine sediments has proven that Fe speciation can provide critical insights for identification of anoxic water columns. Aside from anoxic and fully-oxygenated depositional environments, low-oxygen water columns (dissolved O_2 < 10 μmol/kg) represent another important scenario for oceanic Fe cycling. These water column conditions are usually associated with redox processes in bottom waters and porewaters (e.g., nitrate, Mn, Fe oxyhydroxide, and sulfate reduction) and varied Fe mineral preservation in underlying sediments. Few investigations of Fe speciation exist in highly oscillatory low-O_2 water columns (Raiswell and Canfield, 1998; Scholz et al., 2014) with little attention given to understanding how Fe mineralogy diagenetically shifts down-core under such conditions. Iron mineralogy generated by overlying water columns may

* Corresponding author.
E-mail address: ellawang@umich.edu (Y. Wang).

https://doi.org/10.1016/j.chemgeo.2019.04.018
Received 8 January 2019; Received in revised form 29 March 2019; Accepted 17 April 2019
Available online 26 April 2019
0009-2541/

change in response to post-depositional diagenesis following shifts in porewater redox environments and/or instantaneous depositional events (e.g., flood layers and turbidites), which could obscure geochemical interpretations of ambient redox environments. Finally, there are few calibration studies of Fe speciation where independent mineralogy techniques were employed, all of which limits understanding of Fe proxy behavior in reducing sediments.

To investigate responses of Fe proxies (speciation and mineralogy) to ambient porewater redox conditions on centennial time scales downcore, we examined a recent sedimentary record from Santa Barbara Basin (SBB), California. New insights into the behavior of Fe diagenesis in this continental borderland basin are provided by the prevailing low-oxygen (O_2 < 10 μmol/kg) and sporadically anoxic (no oxygen detected) bottom water conditions. Iron speciation measurements were made on a box core (SPR0901-04BC) to generate a high-resolution down-core geochemical record spanning the last 250 years. Paired to this record, rapid and non-destructive magnetic techniques were employed to identify specific Fe-bearing minerals and to investigate the response of these minerals to ambient porewater redox environments (Liu et al., 2012), thus providing independent Fe mineralogy to validate Fe speciation interpretations. Finally, using redox-sensitive metals (Re, U, Mo) as independent paleo-redox indicators, we compare different approaches to reconstructing DO change in SBB since ~1760 CE. Together, this multi-proxy approach allows us to revisit interpretations of Fe speciation and mineralogy results that have implications for reconstructing past oxygenation of ocean water columns.

2. Background

2.1. Site description

Located in the Southern California Bight, the Santa Barbara Basin is a near-shore silled basin with a maximum depth of ~590 m, and a sill depth of 475 m to the west and 230 m to the east (Fig. 1). Low-oxygen (dissolved O_2 < 10 μmol/kg) subsurface water entering the basin becomes bathymetrically isolated and further depleted by the oxidant demand of high regional primary productivity. Together, these features lead to a low-oxygen water column below 550 m water depth. Prevailing low-oxygen conditions with sporadic anoxia in SBB bottom waters contributes to intensive oxidant substitution near the sediment-water interface (SWI) and the subsequent preservation of laminated sediments (Schimmelmann et al., 1990; Soutar and Crill, 1977). The penetration depth of bottom water oxygen is typically < 1 cm below the SWI in SBB, and a rapid succession of electron acceptors (from NO_3^- to Mn(IV), Fe(III), and SO_4^{2-}) occurs within the upper 5 cm of the sediment (Kuwabara et al., 1999; Reimers et al., 1990; Reimers et al., 1996). Sharp shifts of geochemical gradients in SBB sediments facilitate numerous biogeochemical processes (e.g., denitrification, microbe-mediated iron, manganese, and sulfate reduction), which in turn control redox-sensitive element geochemistry. Biogenic methane – the product of methanogenesis – starts to accumulate in the sulfate methane transition zone (SMTZ) at ~100–150 cm in SBB (Harrison et al., 2009; Komada et al., 2016). Both anoxic oxidation of methane (AOM) and sulfate reduction for anaerobic organic carbon degradation occur within the SMTZ, resulting in continued production of free sulfide (Berelson et al., 2005; Harrison et al., 2009). These low-oxygen yet highly variable bottom water redox environments make SBB an ideal location for examining high-resolution responses of sedimentary redox proxies (iron speciation and redox-sensitive trace metals) to water column DO changes. Typical box core lengths (62 cm for SPR0901-04BC) are insufficient to penetrate to the SMTZ (~100–150 cm depth), and thus diagenetic impacts of additional sulfide production by AOM in SMTZ could not be evaluated.

2.2. Paleo-redox proxies

2.2.1. Iron mineralogy

Preservation of Fe-bearing minerals and their responses to sedimentary diagenesis provide valuable information about redox conditions in their ambient environments. In oxic conditions, Fe (oxyhydr) oxides are frequently found in sediments including amorphous ferrihydrite, lepidocrocite (γ-FeOOH), crystalline and nanoparticulate goethite (α-FeOOH) (Poulton and Raiswell, 2005; van der Zee et al., 2003), hematite (α-Fe_2O_3), maghemite (γ-Fe_2O_3), and magnetite (Fe_3O_4) (Berner, 1981; Schwertmann, 2008). When free sulfide is present in porewaters or the water column, these minerals can be reductively dissolved and progressively converted to Fe sulfides including mackinawite (FeS), greigite (Fe_3S_4), and pyrite (FeS_2), although reactivity toward H_2S varies among different minerals (Poulton et al., 2004; Raiswell and Canfield, 2012; Roberts, 2015). In addition, excessive reactive Fe can be trapped by Fe carbonate ($FeCO_3$, siderite) in strongly reducing conditions, notably in methanic environments where H_2S is absent (Berner, 1981; Roberts, 2015). Porewaters need to be supersaturated in HCO_3^- to form siderite (e.g., during methane oxidation in the presence of Fe(II)); however, these conditions are difficult to achieve in marine environments where sulfate concentrations are frequently high.

2.2.2. Iron speciation

Iron speciation is commonly employed in DO reconstructions

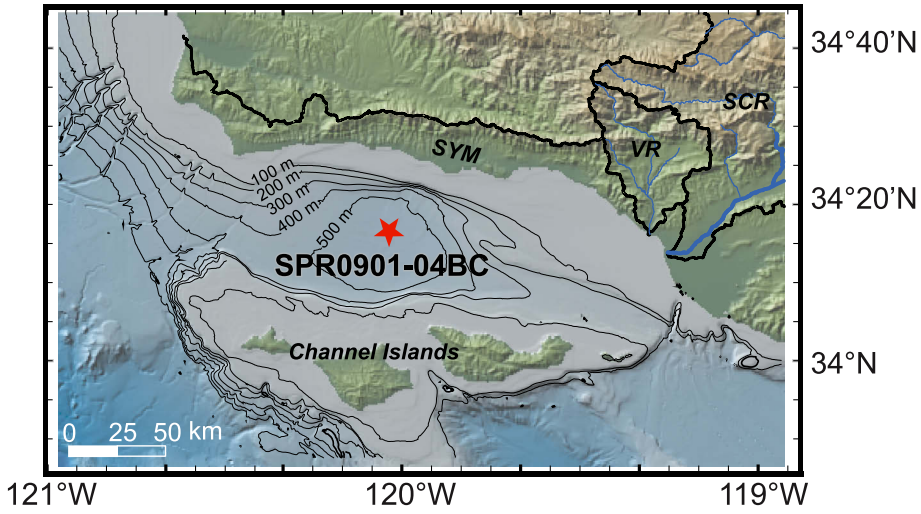

Fig. 1. Map of the Santa Barbara Basin, California. The red star denotes the location of the SPR0901-04BC core site and river catchments are outlined in black: Santa Clara River (SCR), Ventura River (VR), Santa Ynez Mountain (SYM), and Channel Islands. Main stems of selected rivers are indicated by thick blue lines. (For interpretation of the references to colour in this figure legend, the reader is referred to the web version of this article.)

because Fe reduction/oxidation is closely associated with redox potential. This technique extracts four groups of iron minerals (Fe carbonate, Fe oxyhydroxides, magnetite, and pyrite) to target three parameters — Fe_T [total Fe]/Al, Fe_{HR} [highly-reactive Fe]/Fe_T, and Fe_{py} [pyrite Fe]/Fe_{HR} —which can be used to distinguish between oxic, ferruginous, and euxinic conditions (Clarkson et al., 2014; Lyons and Severmann, 2006; Poulton and Canfield, 2011; Poulton and Raiswell, 2005). Carbonate-bearing Fe and Fe (oxyhydr)oxides are commonly considered to be highly reactive because these forms of Fe readily react with HS^- in early diagenetic stages. When combined with pyrite iron (Fe_{py}), carbonate-bearing Fe, and Fe (oxyhydr)oxides are collectively defined as the highly-reactive iron pool (Fe_{HR}) (März et al., 2008a; Poulton and Raiswell, 2005; Raiswell and Canfield, 2012). Fe_{HR}/Fe_T and Fe_T/Al proxies measure authigenic Fe enrichment relative to lithogenic input and are used as anoxia indicators to distinguish oxic from anoxic water columns (Clarkson et al., 2014; Lyons and Severmann, 2006; Raiswell and Canfield, 1998). Calibration studies on modern sediments indicate a threshold of $Fe_{HR}/Fe_T > 0.38$ for anoxic water columns (Poulton and Canfield, 2011; Raiswell and Canfield, 1998), while a lower Fe_{HR}/Fe_T threshold value of 0.22 has been suggested following calibration studies on Phanerozoic rocks (Poulton and Raiswell, 2002). In this study we use the modern anoxic water column calibration ($Fe_{HR}/Fe_T = 0.38$) due to the centennial timescale of our record. Fe_T/Al requires a baseline value to assess enrichments, and oxic Phanerozoic shale values (0.53 ± 0.11) are commonly applied to indicate anoxic environments (Clarkson et al., 2014; Lyons and Severmann, 2006; Poulton and Raiswell, 2005). Nevertheless, local lithogenic background values of Fe_T/Al should be used when location-specific anoxic thresholds are available (Clarkson et al., 2014; Lyons and Severmann, 2006), and thus a local anoxia threshold $Fe_T/Al = 0.54$ is used. This threshold is based on geochemical analysis of silt sized (grain size < 63 μm) SBB river sediments adjusted for catchment contribution to SBB (Wang et al., 2017). Fe_{py}/Fe_{HR} measures the extent to which highly-reactive iron is sulfidized to pyrite. Under anoxic regimes ($Fe_{HR}/Fe_T > 0.38$), Fe_{py}/Fe_{HR} can differentiate euxinic ($Fe_{py}/Fe_{HR} > 0.7$–0.8, free sulfide present) from ferruginous ($Fe_{py}/Fe_{HR} < 0.7$, anoxic with free Fe(II) present) water columns (Clarkson et al., 2014; Li et al., 2015; März et al., 2008b; Poulton and Canfield, 2011; Poulton et al., 2015). When $Fe_{HR}/Fe_T < 0.38$, high Fe_{py}/Fe_{HR} values (> 0.8) have also been used to indicate oxic water columns with porewater sulfide accumulation in organic carbon-rich sediments (e.g., the Friends of Anoxic Mud site (FOAM), Canfield et al. (1992); Hardisty et al. (2018); Raiswell and Canfield (1998); Raiswell et al. (2018)).

2.2.3. Trace metal enrichments

Independent of Fe proxies, redox-sensitive metals - notably Mn, Re, U, and Mo - can be used to reconstruct redox conditions, because their geochemical behavior differs as DO conditions change. In the presence of oxygen, Mn exists as insoluble Mn(IV) oxides and is readily scavenged into sediments; whereas in reducing environments, Mn (oxyhydr)oxides are subject to reductive dissolution to form Mn(III)-L (soluble Mn(III) complexed by inorganic or organic ligands) in low-oxygen porewaters (Madison et al., 2013) and to Mn(II) which can diffuse out of sediments as porewaters become more reducing. Thus, sedimentary Mn enrichment is frequently used to support an oxygenated water column (Calvert and Pedersen, 2007). Used jointly, multiple redox-sensitive elements (proxy suites) can improve interpretations of redox conditions. For example, free Mn(II) can also precipitate as $MnCO_3$ and/or co-precipitate with authigenic calcite in reducing porewaters with high alkalinity (Calvert and Pedersen, 1996; Mucci, 2004) to provide a false positive for oxic conditions, and thus Mn should be evaluated simultaneously with other redox-sensitive elements. Both Re and U have low detrital flux and behave conservatively in oxygenated waters (existing as ReO_4^- and $UO_2(CO_3)_2^{2-}$, respectively), and therefore are frequently used as tracers of low-DO conditions (Crusius and Thomson, 2000; Hendy and Pedersen, 2005; McManus et al., 2005; Morford and Emerson, 1999). In low-oxygen waters, Re and U have similar redox potentials and tend to be significantly enriched compared to crustal values as reduction produces Re(IV) oxides/sulfides and U(IV) precipitates (Calvert and Pedersen, 2007; Crusius et al., 1996; McManus et al., 2006; Tribovillard et al., 2006). Additionally, Re preservation in sediments may be associated with thiolation of ReO_4^- to particle-reactive $ReO_nS_{4-n}^-$ and/or co-precipitation with the Fe-Mo-S phase in sulfidic waters. However, free sulfide levels in most euxinic water columns are usually insufficient to support thiolated ReO_4^- as major species (Helz and Dolor, 2012; Vorlicek et al., 2015).

Molybdenum primarily behaves conservatively in oxygenated water columns in the form of molybdate (MoO_4^{2-}) despite co-precipitation with Mn (oxyhydr)oxides (Scott et al., 2008; Tribovillard et al., 2006). In contrast to Re and U, however, Mo precipitation requires the presence of free sulfide (Crusius et al., 1996; Zheng et al., 2000). A key step in converting unreactive molybdate to authigenic Mo is the progressive formation of a thiomolybdate series ($MoO_xS_{4-x}^{2-}$, x = 0–4) in the presence of free sulfide (Erickson and Helz, 2000; Helz et al., 1996; Tribovillard et al., 2006; Vorlicek et al., 2004), which are highly particle-reactive and readily scavenged into sediments. The subsequent removal/sequestration is thought to be associated with Fe-Mo-S cluster formation (Helz et al., 2011) and/or absorption onto sulfide-rich organic matter (Helz et al., 1996). Since the rate of Mo scavenging in sulfidic environments is significantly faster than in oxic ones, Mo enrichment is interpreted as an indicator of euxinic environments provided that coeval U enrichments are observed (Calvert and Pedersen, 2007; McKay et al., 2007; Scott et al., 2008; Tribovillard et al., 2006).

3. Methods

Box core SPR0901-04BC (34° 16.895′ N, 120° 02.489′ W, 588 m water depth) was collected in SBB in January 2009. The core contains an olive layer deposited by a turbidite associated with the 1812 Santa Barbara earthquake at a depth of 43–49 cm below the core top (cmbct) and two gray layers associated with flood events (a 0.7-cm-thick layer dated to 1861–62 CE at 38 cmbct and a 1.5-cm-thick layer dated to 1761 at 59 cmbct; Hendy et al. (2015)). SPR0901-04BC was stored at 4 °C until core splitting took place in January 2010. Porewater loss was observed in the cold room but visual inspections upon core splitting confirmed that the core interior had maintained its original appearance with dark sulfide-rich laminations. The split cores were encased in multiple layers of plastic wrap to minimize evaporation during storage at 4 °C. In 2013, the core was sampled at continuous 1-cm intervals (capturing ~2–7 years per sample) to obtain 62 bulk sediment samples. Discrete samples were immediately frozen to avoid oxidation and were then freeze-dried. Dried samples were ground to < 75 μm for geochemical and magnetic analyses.

3.1. Magnetic measurements

Magnetic measurements on discrete freeze-dried samples were conducted at the Institute for Rock Magnetism, University of Minnesota. Magnetic measurements are summarized here. Detailed procedures are given in Supplementary Materials. To quantify concentrations of magnetic minerals in bulk sediments, low-field mass magnetic susceptibility (χ) was determined at 1-cm intervals using an AGICO Kappabridge MFK1 susceptometer at room temperature, followed by measurements of anhysteretic remanent magnetization (ARM) and saturation isothermal remanent magnetization (SIRM, after application of a 1 T direct current field) on a 2G Enterprises superconducting quantum interference device (SQUID) passthrough magnetometer located in a magnetically shielded laboratory. ARMs were imparted using a 0.1 mT DC bias field and a 100 mT alternating field (AF).

Magnetic hysteresis properties were measured to produce first-order reversal curve (FORC) diagrams to illustrate the magnetic domain state of magnetic minerals and to allow further insights into Fe mineralogy.

Hysteresis loops were measured on a Princeton Measurements Corporation MicroMag vibrating sample magnetometer (VSM) at room temperature with a maximum field of 1 T. Saturation magnetization (M_s), saturation remanence (M_{rs}), coercive force (B_c), and coercivity of remanence (B_{cr}) were determined from hysteresis loops (after a paramagnetic slope correction following Jackson and Solheid (2010)) and back-field remanence curves. 'Hard' isothermal remanent magnetization (HIRM, (SIRM + IRM_{-300})/2) and S-ratio ($S_{-300} = -IRM_{-300mT}$/SIRM) were obtained from hysteresis measurements. The L-ratio was then calculated following Liu et al. (2007) as HIRM / [0.5 × (SIRM + IRM_{-100mT})], which is used to demonstrate relative contributions from hard (saturation field > 300 mT) with respect to intermediate-coercivity (saturation field between 100 mT and 300 mT) magnetic minerals. Additionally, first-order reversal curve (FORC) diagrams (Pike et al., 1999; Roberts et al., 2014; Roberts et al., 2000) were determined for selected samples on the VSM with an averaging time of 1–1.5 s and a saturating field of 0.7 T. On average, 170–200 individual FORCs were acquired for each sample. FORC diagrams were calculated and optimized using the variable smoothing approach (VARIFORC) (Egli, 2013) in the FORCinel package 3.0.3 (Harrison and Feinberg, 2008).

Temperature-dependent magnetic properties were also measured on selected samples to identify magnetic minerals with characteristic low-temperature transitions. Low-temperature measurements were undertaken using a Quantum Design Magnetic Properties Measurement System (MPMS-5S). For zero-field-cooled (ZFC) and field-cooled (FC) remanence curves, samples were cooled to 10 K either in the absence of a magnetic field (ZFC) or in the presence of a 2.5 T field (FC). For FC measurements, the 2.5 T field was then switched off and the magnetic remanence was measured upon warming back to room (300 K) temperature in 5 K intervals. For ZFC, a low-temperature SIRM (LTSIRM) was imparted at 10 K, and remanence was measured every 5 K during warming. For low temperature cycling (LTC) remanence curves, a room temperature SIRM (RTSIRM) was first imparted on the sample, then the remanence was measured at 5 K steps during cooling (from room temperature to 10 K) and warming back to 300 K in a zero field. High-temperature measurements were performed on a Kappabridge susceptometer. For each sample run, ~200–300 mg of sample was weighed, heated from room temperature to 700 °C in air, and cooled to room temperature while measuring χ in 3 °C steps.

3.2. Iron speciation

The iron speciation method used has been adapted from the sequential Fe extraction protocol of Poulton and Canfield (2005) and chromium reducible sulfide extraction (CRS) following Canfield et al. (1986). Sequential Fe extraction was performed on 150–200 mg of the bulk sediment sample, and a further ~300 mg of the sample was used to trap chromium reducible sulfides. This procedure operationally defines four Fe pools as listed in Table 1. Each step in the sequential Fe extraction (the first three steps) was followed by centrifugation on a Thermo Scientific Sorvall Legend XT system (with the Thermo Scientific TX-750 rotor) at 3500 rpm (2684 × *g*) for 5 min before proceeding to the next treatment. Iron extracted in sequential Fe extraction was determined on a Perkin Elmer Optima 2100 DV inductively-coupled plasma optical-emission spectrometer (ICP-OES) at Indiana State University. Prior to analyzing the samples, optics were peaked using a 1 ppm Mn solution. Fe concentrations were determined following a standard 4-point calibration curve from a Perkin Elmer stock standard solution. Analytical precision was evaluated by comparison with replicate samples, which all agreed within 10%. Analytical accuracy was determined by incorporating known samples into the analysis and knowns agreed within 2%. The analytical detection limit for Fe was 0.06 ppm.

Operationally CRS measures ZnS precipitated from chromium reducible sulfide, which extracts all inorganic sulfur, including acid-volatile sulfur (AVS, e.g., mackinawite, pyrrhotite, and greigite), elemental sulfur (S^0), and pyrite. AVS extraction was not attempted because only freeze-dried samples were available, and thus AVS oxidation/loss during freeze-drying could not be excluded. CRS, as an alternative, measures all inorganic sulfur species and it is unaffected by potential Fe sulfide oxidation. Replicates on selected samples (15% of total samples) agree within ~6%. Previous work has shown that AVS is oxidized to a phase (e.g., elemental sulfur) that can still be extracted by CRS (Canfield et al., 1986; Lyons and Severmann, 2006; Raiswell and Canfield, 1998). In observational data, pyrite-bound sulfur always dominates inorganic sulfur in SBB with minor AVS (AVS-S/pyrite-S values of 0.06–0.12, Kaplan et al. (1963); Rickard and Morse (2005)) and negligible elemental sulfur contributions (< 2% of the total sulfur, Kaplan et al. (1963)), and thus the stoichiometrically determined pyrite-associated iron (Fe_{py}) from CRS provides the maximum pyrite abundance in the core with likely significant overestimation near the core top (Canfield et al., 1986). Highly-reactive Fe (Fe_{HR}) is thus defined as $Fe_{ace} + Fe_{dith} + Fe_{ox} + Fe_{py}$, which corresponds to Fe carbonate, Fe (oxyhydr)oxides, and pyrite. Total Fe (Fe_T) in bulk sediment was determined by ICP-MS and ICP-OES at ALS Laboratories in Vancouver, British Columbia (Hendy et al., 2015). Samples were digested with a hydrofluoric, nitric, perchloric, and hydrochloric cocktail. Lab standard (GBM908-10 and MRGeo08) replicates were used to verify elemental concentrations, and agreed within 2%. Unreactive silicate bound Fe (Fe_{UR}) is only reactive on 10^6-year or longer time scales and is determined from Fe_T-Fe_{HR}. Although the CRS protocol also extracts sulfur bound to other trace metals, this additional contribution should be negligible due to relatively low concentrations of those metals (März et al., 2008a). Possible core oxidation will not affect Fe_{HR} and Fe_T measurements as oxidized Fe sulfides can be extracted as Fe_{dith} (Raiswell and Canfield, 1998).

To assess the extent of core oxidation after collection, Fe_{dith} in this study is compared to Raven et al. (2016), where dithionite extraction was performed on SBB sediments stored under nitrogen (Table S2). Near the core top (above 23.5 cm), the two datasets agree within 10%. Higher Fe_{dith} values observed down-core (below 23.5 cm) in 04BC, relative to Raven et al. (2016), might result from pyrite oxidation. However, as CRS measures inorganic sulfur dominated by pyrite, the down-core Fe_{py} record should not be significantly altered. Additionally, possible Fe (oxyhydr)oxide inputs by instantaneous depositional events, inter-core variability, and seasonal changes in bottom water and porewater environments cannot be excluded and may have led to

Table 1
Iron speciation procedure and intended target phases.

Extraction procedure	Intended extracted Fe phases
10 mL 1 M sodium acetate solution (pH 4.5; buffered with acetic acid; shake for 24 h)	Fe_{ace}: Fe bound with carbonate
10 mL 50 g L^{-1} sodium dithionite solution (pH 4.8; buffered with 0.35 M acetic acid and 0.2 M sodium citrate; shake for 2 h)	Fe_{dith}: Fe (oxyhydr)oxides, (e.g., ferrihydrite, lepidocrocite, goethite, and hematite)
10 mL 0.2 M ammonium oxalate, and 0.17 M oxalic acid solution (pH 3.2, buffered with ammonium hydroxide, shake for 6 h)	Fe_{ox}: magnetite
40 mL 1 M $CrCl_2$ solution acidified to 0.5 M HCl (boiling for 2 h; bubbled with N_2, H_2S precipitated in zinc acetate trap)	Fe_{py}: assume that all chromium reducible sulfur is bound as pyrite

Table 2
Magnetic properties for iron minerals (following Hunt et al. (1995)).

Mineral	Magnetic properties	Saturation field (T)	Saturation magnetization (M_s, Am^2/kg)	Low-T cycling	Curie/Néel temperature (°C)
Magnetite (Fe_3O_4)	Ferrimagnetic		90–92	~120 K (Verwey transition, T_v)	580
Goethite (α-FeOOH)	Antiferromagnetic	Very high (> 1 T), B_c tail to > 700 mT in FORC distribution (Roberts et al., 2006)	~0.5	Large difference between FC and ZFC, with large (×2) and reversible RTSIRM increase at low-T (Dekkers, 1989a; Liu et al., 2006)	120 (Özdemir and Dunlop, 1996)
Hematite (α-Fe_2O_3)	Antiferromagnetic at room temperature	High, B_c tail to > 150 mT in FORC distribution (Roberts et al., 2006)	~0.5	260 K (Morin transition)	675
Maghemite (γ-Fe_2O_3)	Ferrimagnetic	A quasi-circular peak centered at B_c = ~40 mT in FORC for SD particles (Carvallo et al., 2004)	~80	Hump-shaped RTSIRM curves (Özdemir and Dunlop, 2010)	645 (Özdemir and Banerjee, 1984)
Pyrite (FeS_2)	Paramagnetic				
Greigite (Fe_3S_4)	Ferrimagnetic	B_c peak at 70–85 mT for SD particles (Roberts et al., 2006)	~25	No transitions (Chang et al., 2009)	> 400 (Roberts et al., 2011)
Pyrrhotite ($Fe_{1-x}S$)	Ferrimagnetic (monoclinic)		~20	Besnus transition at 34 K for monoclinic type (Dekkers, 1989b) but no transition for hexagonal type (Horng and Roberts, 2018)	
Siderite ($FeCO_3$)	Paramagnetic			Sharp decay in FC warming curve until 37 K (Frederichs et al., 2003)	

higher Fe_{dith} values in this study.

4. Results

4.1. Magnetic measurements

Magnetic properties used for Fe mineral identification are summarized in Table 2. High-temperature magnetic susceptibilities suggest that Fe sulfide is present (e.g., pyrite) throughout the core (Fig. S3) (Passier et al., 2001), but neither siderite nor pyrrhotite are present in significant concentrations based on results from ZFC and FC remanence curves (Fig. S1). Low-temperature cycling of a RTSIRM also indicates the presence of magnetite, maghemite, and a small amount of goethite, as do the FC-ZFC curves (Supplementary material, Figs. S1 and S2). Based on down-core changes in magnetic mineralogy and magnetic mineral concentrations, the core has been subdivided into three distinct zones defined by a gradual decrease of stable magnetic minerals, coercivity (concentration-independent) shifts, and magnetic grain size changes (Supplementary material).

In Zone 1 (0–35 cm below core top, cmbct), samples contain relatively high concentrations of stable ferrimagnetic minerals (Fig. 2). Notably, there is a significant contribution from single domain/vortex state (SD/vortex) mixtures of maghemite (formed by magnetite oxidation) in addition to biogenic and inorganic magnetite (Figs. 3, S1, and S3) (Roberts et al., 2017; Roberts et al., 2018). Interactive SD behavior in Zone 1 (e.g., 15–16 cm) could be attributed to collapse of biogenic magnetite chains (Harrison and Lascu, 2014). A trend toward coarser-grained ferrimagnetic Fe oxides with depth in Zone 1 is also indicated by the increased distribution along the B_u axis in the FORC diagrams (Fig. 3).

In Zone 2 (Fig. 2, 35–56 cmbct), samples undergo a major transition toward significantly lower magnetic mineral concentrations and a coarser magnetic grain size distribution (Fig. S1). The dominant SD/vortex state mineral assemblages found in the core top are gradually replaced by vortex state/multi-domain (vortex/MD) magnetic minerals (Fig. 3) with an additional relatively higher contribution from high-coercivity minerals (e.g., hematite, Fig. 2h). Low-temperature measurements also reveal increased coarse detrital magnetite concentrations in sediments from the two instantaneous depositional events (Fig. S1, the olive turbidite layer associated with the 1812 Santa Barbara earthquake, and the 1861–62 gray layer associated with a flood deposit, Hendy et al. (2015)).

Samples in Zone 3 (Fig. 2, 56–61 cmbct) have the lowest concentrations of magnetic minerals, yet the highest contribution of high-coercivity Fe oxides like hematite (Fig. 4). Similar to other instantaneous sediment depositional events in Zone 2, the 1.5-cm-thick gray layer associated with the 1761 flood (Hendy et al., 2015) exhibits coarser magnetic grain sizes and an abrupt but small increase in high-coercivity minerals (Figs. 2 and 4). Nevertheless, the slope (95% confidence level) of the L-ratio regression line in Zone 3 is significantly higher than in Zone 2, indicating deposition of a 'harder' (higher-coercivity) mineral assemblage in the Zone 3 flood layer (1761 CE) relative to the turbidite (Fig. 4). Additionally, a reversal trend to lower B_{cr}/B_c values is observed in Zone 3. Similar trends have been reported in reducing diagenetic environments, including the northern California and Oman margins (Roberts, 2015; Rowan et al., 2009), where the reversal is associated with growth of SP greigite into the stable SD particles. Although SP greigite formation could occur, there is little evidence for a significant SD greigite contribution in Zone 3 as S-ratio and ARM/SIRM do not increase down-core (except the last data point, Fig. 2h and f), which would occur if 'soft' ferrimagnetic minerals have increased contributions (see Supplementary Materials). Complete descriptions of the magnetic measurements are provided in Supplementary Materials.

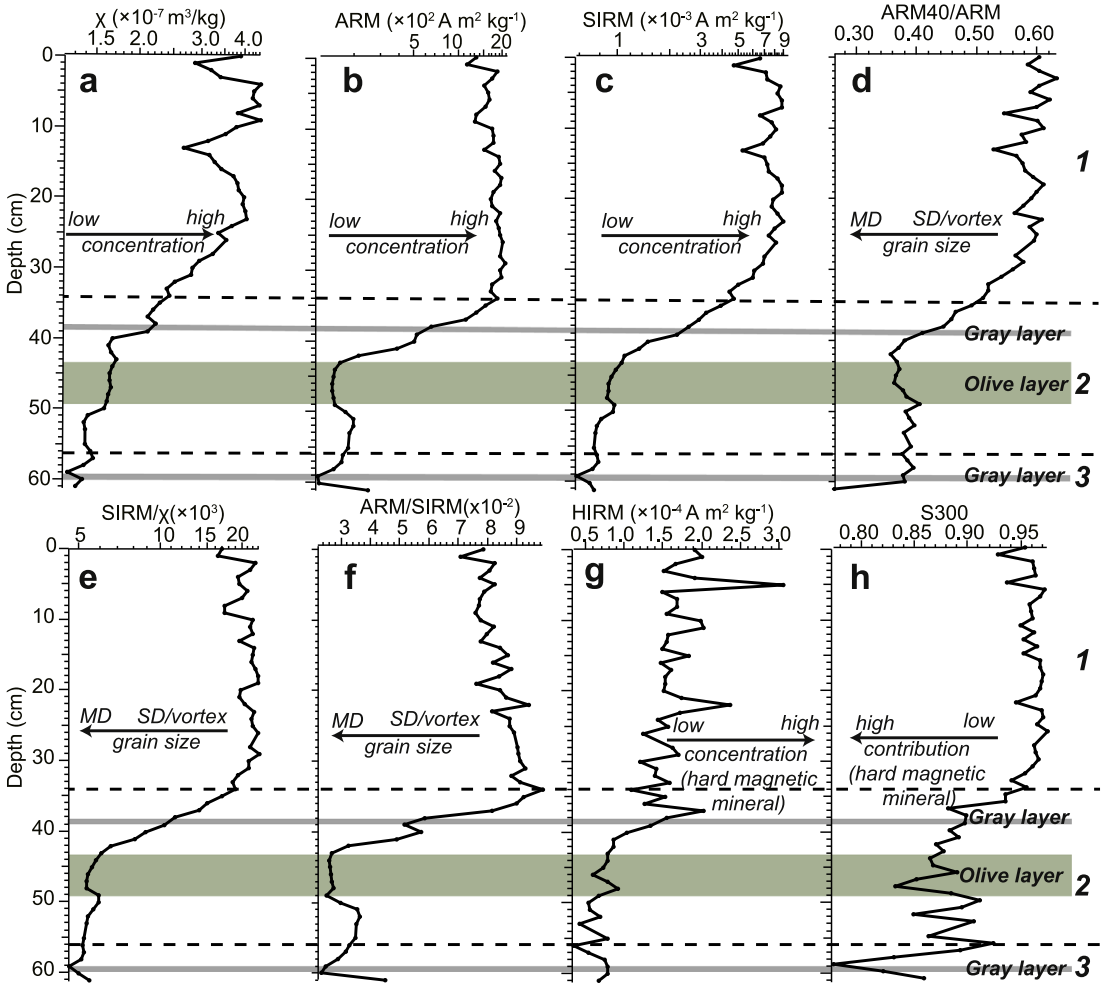

Fig. 2. Down-core comparison of magnetic parameters for SPR0901-04BC from the Santa Barbara Basin. (a) Magnetic susceptibility χ; (b) anhysteretic remanent magnetization (ARM); (c) saturation isothermal remanent magnetization (SIRM); (d) ARM40 (ARM after demagnetization at 40 mT)/ARM; (e) SIRM/χ; (f) ARM/SIRM; (g) hard isothermal remanent magnetization (HIRM); (h) S300. Zonation (dashed lines) based on changes in magnetic mineral concentrations and concentration-independent properties is as follows: Zone 1 (0–35 cmbct), Zone 2 (35–56 cmbct), and Zone 3 (56–61 cmbct). Gray and olive layers are shaded in gray and dark green, respectively. Arrows indicate higher concentrations of magnetic minerals (a–c), larger magnetic grain sizes (d–f), higher concentrations of hard magnetic materials (g) or higher contributions from magnetically hard minerals (h). Susceptibility χ, ARM, SIRM, and SIRM/χ are plotted on logarithmic scales. (For interpretation of the references to colour in this figure legend, the reader is referred to the web version of this article.)

4.2. Geochemical Fe speciation

Carbonate-bound Fe isolated by acetate-extracted Fe (Fe_{ace}) varies from 0.02 to 0.20 wt%, with the highest value occurring at the top of the core (Fig. 5a). Below 2 cm, Fe_{ace} sharply decreases and then oscillates within the range of ~0.04–0.15 wt%. Minima occur in all three instantaneous sediment deposition events. A major decrease is observed below the gray layer at 38 cm, while the lowest value occurs within the olive layer (Fig. 5a). Below this layer, Fe_{ace} returns to values similar to Zone 1 samples, but declines again at 54 cm in association with the gray layer at 59–60 cm. Relative to Fe_{ace}, Fe (oxyhydr)oxides extracted by dithionite (Fe_{dith}) are more significant contributors to the reactive iron pool (Fe_{HR}). Although concentrations are more variable (0.10–0.87 wt % range), dithionite-extracted Fe typically accounts for ~30–60% of reactive iron (Table S2). Fe_{dith} undergoes a gradual yet highly variable decline from 0.66 to 0.31 wt% through Zones 2 and 3 (Fig. 5b). Concentrations of oxalate-extracted Fe (Fe_{ox}, likely associated with magnetite) are comparable to Fe_{ace} and range between 0.01 and 0.20 wt% with no significant trend down-core (Fig. 5c).

Chromium reducible sulfur is used to represent Fe bound in pyrite (Fe_{py}) due to pyrite dominance. Fe_{py} generally follows the opposite trend to Fe_{ace} (correlation coefficient $r = -0.4531$, $p = 0.0004$), with the lowest values occurring at the core top (0.05 wt%) and a local maximum at 10 cm (Fig. 5d). Below 13 cm, Fe_{py} returns to ~0.10–0.30 wt% in Zone 1 but increases again in Zone 2, reaching a maximum value of 1.00 wt% above the olive layer (43 cm). In contrast to Fe_{ace}, local Fe_{py} maxima occur within both gray and olive layers. Unreactive iron (Fe_{UR}) is consistently dominant with a > 50% contribution to the total Fe throughout the core (Fig. 5e), and local maxima are shown in both gray layers. The olive layer, however, has two local minimum Fe_{UR} values at its top and bottom (2.12 and 1.93 wt%, respectively) but Fe_{UR} values (~2.6 wt%) remain consistent with background values within this layer (Fig. 5e).

An indicator of Fe enrichment – Fe_T/Al – suggests sustained elevated Fe preservation with respect to the local lithogenic background of 0.54 (Wang et al., 2017) with a range of 0.50–0.68 (Fig. 5f). The uppermost 2 cm has the highest Fe_T/Al ratio, below which Fe_T/Al varies around 0.6. There is no consistent trend down-core but declines are observed in instantaneous depositional events (gray and olive layers), notably a sharp decrease at the bottom of the olive layer where Fe_T/Al reaches its minimum value of 0.50. Although Fe enrichment is observed throughout the core, Fe_{HR}/Fe_T values are usually below the proposed anoxic threshold of 0.38 (Anderson and Raiswell, 2004; Canfield et al., 2007; Poulton and Canfield, 2011). Exceptions occur at 10 cm, 43 cm

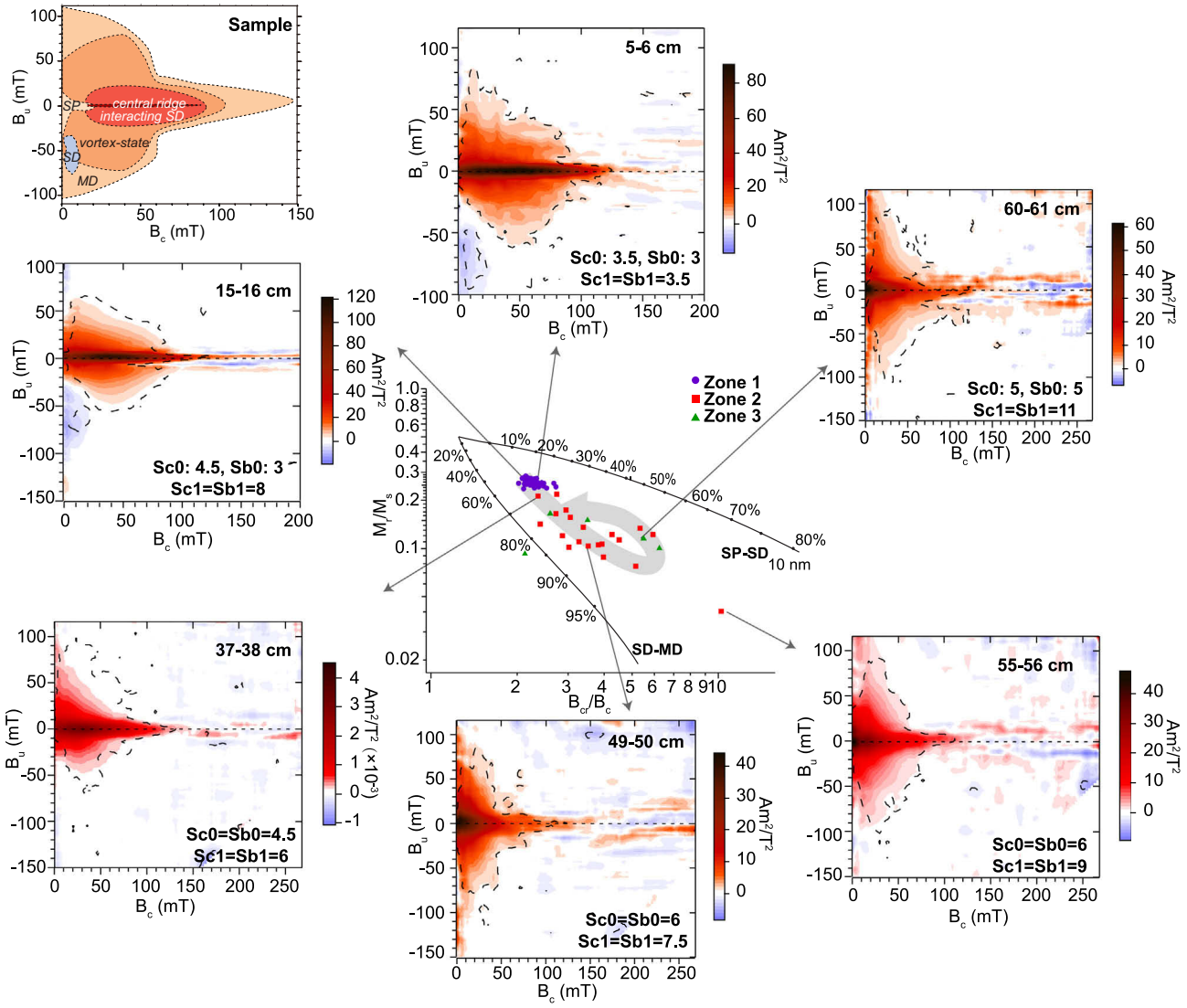

Fig. 3. Day plot (Day et al. (1977)) and FORC distributions for selected samples from SPR0901-04BC. Samples from the three magnetic mineral zones are represented by purple circles (Zone 1: 0–35 cmbct), red squares (Zone 2: 35–56 cmbct), and green triangles (Zone 3: 56–61 cmbct), respectively. The Day plot is used to evaluate the down-core variation of hysteresis parameters. Theoretical SD-MD and SD-SP mixing lines for (titano-)magnetite are modified from Dunlop (2002) and are plotted for reference only. Selected FORC diagrams in each zone are shown surrounding the Day plot to further demonstrate mineralogy shifts down-core. A sample FORC distribution is shown on the top left to demonstrate typical patterns for different domain sizes following Roberts et al. (2014). Depths and VARIFORC parameters (Sc0, Sc1, Sb0, and Sb1) used are indicated on each FORC distribution following Egli (2013), and black dashed lines indicate 95% confidence envelope of the data. (For interpretation of the references to colour in this figure legend, the reader is referred to the web version of this article.)

(top of the olive layer), and 55 cm, with the highest value (0.44) corresponding to the maximum Fe_{py} value at 43 cm (Fig. 5g). Local maxima are observed at the base of all three instantaneous depositional events and at the top of the turbidite. Finally, the proposed euxinic indicator (Fe_{py}/Fe_{HR}) ranges from 0.05 to 0.68, with the lowest values at the core top (0–10 cm) and the highest at the top of the olive layer (Fig. 5h). Again, discrete Fe_{py} maxima occur within the gray layers (Fig. 5d). The depositional redox environments according to the Fe proxies are summarized in a cross plot of Fe_{HR}/Fe_T and Fe_{py}/Fe_{HR} (Fig. 6). Most data fall within the oxic regime with the notable exception of three samples at 10, 43, and 55 cm, of which the 43-cm sample corresponds to the top of the olive layer. No systematic shifts between zones defined by magnetic parameters are observed in the cross plot.

5. Discussion

5.1. Iron mineral identification from magnetic measurements

As magnetic measurements target specific Fe-bearing minerals, additional down-core mineralogical information can be used to constrain and inform geochemical Fe speciation results (summarized in Fig. 7). Both magnetic and Fe speciation measurements indicate that Fe oxides remain present throughout the core, yet magnetic measurements identify specific Fe-bearing mineral sources (e.g., maghemite and biogenic magnetite) that are not specifically targeted and/or addressed by Fe speciation techniques. Dithionite-extractable iron (Fe_{dith}) in sequential Fe extraction is often interpreted as the hematite and goethite contribution to the Fe mineral pool (Poulton and Raiswell, 2005; Tessin et al., 2016). In SBB sediments, magnetic measurements indicate only a minor contribution from hematite and goethite (especially in Zone 1, Supplementary material), consistent with previous southern California Borderland basin studies (Leslie et al., 1990).

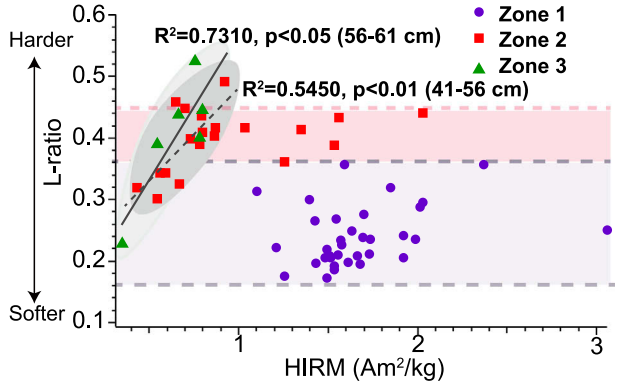

Fig. 4. Cross-plot of magnetic parameters, L-ratios, and HIRM for core SPR0901-04BC. Samples from the three magnetic mineral zones are denoted by purple circles (Zone 1: 0–35 cmbct), red squares (Zone 2: 35–56 cmbct), and green triangles (Zone 3: 56–61 cmbct), respectively. The light purple and red shaded rectangles represent subsets of data for which L-ratios and HIRM are not correlated in Zone 1 and Zone 2, respectively. The dark and light gray shaded eclipses indicate subsets of data whose L-ratios and HIRM are correlated in Zone 2 and Zone 3. The gray dashed line and solid line represent the linear regression lines for data included by shaded eclipses for the Zone 2 (41–56 cm, including an olive turbidite layer at 43–49 cm) and Zone 3 (56–61 cm, including a gray flood layer at 59–60 cm), respectively. R^2 and p-values with depths for each zone are shown beside the regression lines. Correlations between L-ratios and HIRM indicate variable hematite coercivity and the possibility of hematite source shifts in the sediment record. (For interpretation of the references to colour in this figure legend, the reader is referred to the web version of this article.)

Given that Fe_{dith} remains a significant contributor to Fe_{HR} (~30–60%, Table S2 and Fig. 5b), minerals other than hematite or goethite have likely been extracted as Fe_{dith} during sequential digestion. Hump-shaped RTSIRM curves and the shape of high-temperature χ curves suggest a significant contribution from maghemite (γ-Fe_2O_3) formed by magnetite oxidation (Figs. S1 and S3) (Chang et al., 2013; Özdemir and Dunlop, 2010). It is possible that Fe_{dith} reflects the presence of maghemite resulting from magnetite oxidation as the core was exposed to O_2 in storage, especially near the core top where magnetite oxidation is more significant (Supplementary Materials, Fig. S2). However, Fe_{dith} values in 04BC are similar to a nearby multicore that was stored under N_2 (Raven et al., 2016), which argues against maghemite formation from core oxidation (Table S1). Instead, the significant contribution of maghemite with minor contributions from goethite and hematite in Fe_{dith} is likely sourced from detrital lithogenic sediments. With the same chemical formula as hematite (α-Fe_2O_3) but a different crystal structure, maghemite preservation has likely been overlooked in sulfidic marine environments.

Both FC and ZFC remanence curves contain a double-peak Verwey transition (T_v) feature (at ~100 °C and 120 °C), indicating the possible existence of biogenic magnetite near the core top (Fig. S1, Zone 1) (Chang et al., 2016a). Transmission electron microscope (TEM) observations confirm the presence of intact cuboidal or prismatic single domain (SD) biogenic magnetite crystal chains in surficial SBB sediments (Chang and Kirschvink, 1989; Stolz et al., 1986). These observations are consistent with the 'central ridge' feature in FORC diagrams for the samples near the SWI (e.g., Egli et al. (2010); Roberts et al. (2012), Fig. 3), further corroborating the presence of biogenic magnetite in Zone 1 of the SBB sediments (Fig. S1). Similar patterns in FC and ZFC derivatives have been reported in north Arabian Sea oxygen minimum zone sediments (Chang et al., 2016a; Chang et al., 2016b) associated with sulfidic porewater environments similar to SBB.

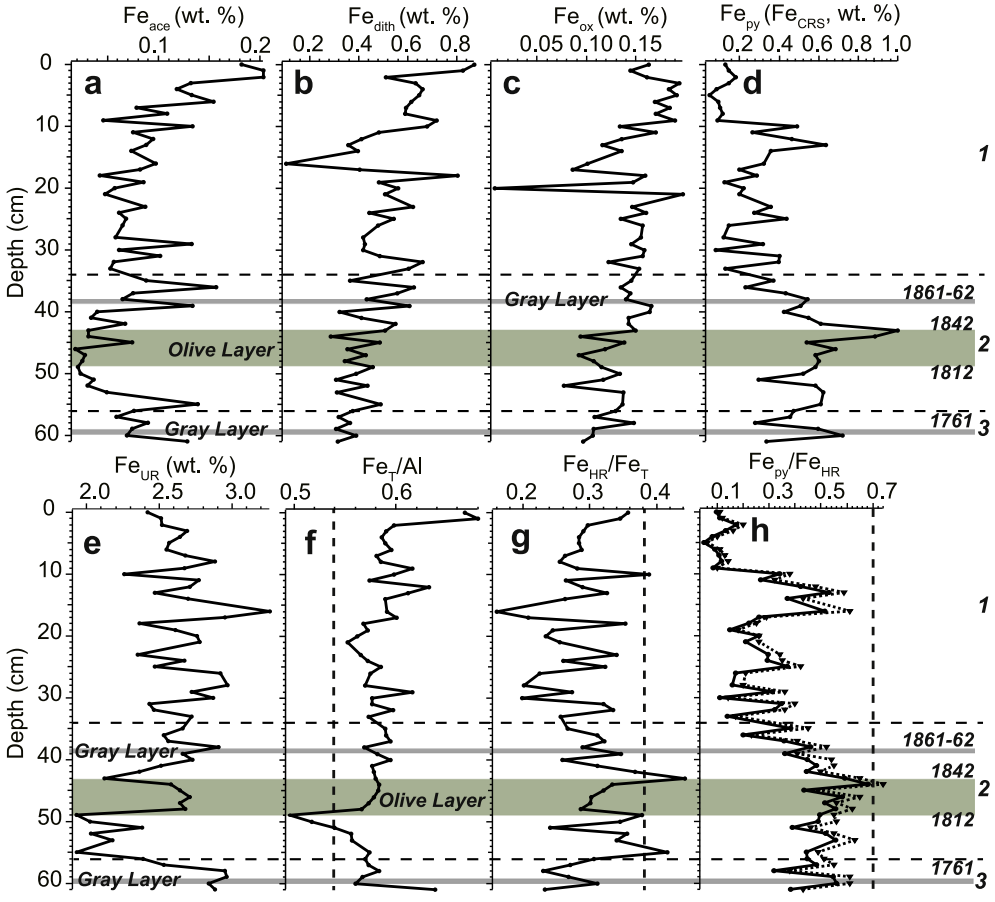

Fig. 5. Down-core comparison of iron speciation profiles in SPR09091-04BC. (a) acetate extracted iron (Fe_{ace}); (b) dithionite extracted iron (Fe_{dith}); (c) oxalate extracted iron (Fe_{ox}); (d) chromium-reducible sulfur bound iron (Fe_{py} when assumed to be in pyrite form with stoichiometry of Fe:S = 1:2); (e) unreactive iron (presumed to be silicate bound iron); (f) Fe_T (total iron)/Al, and the vertical dashed line shows the crustal value of 0.54; (g) Fe_{HR} (highly-reactive iron)/Fe_T, and the vertical dashed line denotes the anoxic threshold of 0.38; (h) Fe_{py}/Fe_{HR}. The dashed line denotes the high-FeS_2 (pyrite) scenario, where all magnetite is assumed to form from pyrite oxidation to demonstrate possible core oxidation effects. Zonation (dashed lines) based on changes in magnetic mineral concentrations and concentration-independent properties is as follows: Zone 1 (0–35 cmbct), Zone 2 (35–56 cmbct), and Zone 3 (56–61 cmbct). Gray bars represent gray layers (1761 CE and 1861–1862 CE) in the core while the turbidite layer (1812–1842 CE) is shaded in dark green. (For interpretation of the references to colour in this figure legend, the reader is referred to the web version of this article.)

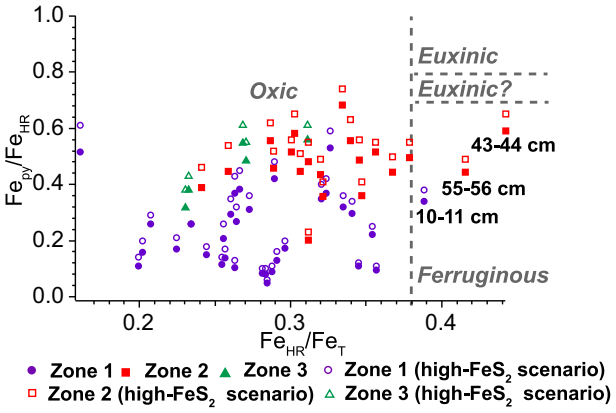

Fig. 6. Cross-plot of Fe_{py}/Fe_{HR} vs. Fe_{HR}/Fe_T in core SPR0901-04BC. Samples from the three magnetic mineral zones are represented by purple circles (Zone 1: 0–35 cmbct), red squares (Zone 2: 35–56 cmbct), and green triangles (Zone 3: 56–61 cmbct), respectively. The hollow markers represent the high-FeS_2 (pyrite) scenario. The vertical dashed line indicates the threshold between oxic and anoxic water columns (Fe_{HR}/Fe_T = 0.38), respectively. In the anoxic regime, the horizontal dashed lines denote the threshold of euxinia at Fe_{py}/Fe_{HR} = 0.7–0.8. Depths for the three data points in the ferruginous region are indicated. (For interpretation of the references to colour in this figure legend, the reader is referred to the web version of this article.)

Together, these observations indicate that biogenic magnetite preservation in low-oxygen (suboxic) sedimentary environments might be more common than predicted by abiotically-controlled geochemistry in reducing environments, on the decadal to centennial timescale of recent/modern sediments. However, fine-grained biogenic magnetite remains unstable in sulfidic porewater environments (e.g., the lack of double-peak T_v in Zone 2 and 3), and should be dissolved completely as diagenesis continues (e.g., additional sulfide production in SMTZ via AOM and anaerobic organic carbon degradation) over longer time scales (Roberts, 2015). Further study of Fe minerals over millennial- and longer time scales is needed, however, to support biogenic magnetite preservation under sulfidic porewater conditions in the geologic record.

Biogenic magnetite production has been attributed to either biologically-controlled mineralization by magnetotactic bacteria or biologically-induced mineralization by dissimilatory Fe-reducing bacteria. Magnetotactic bacteria produce magnetite with highly-controlled grain sizes and morphology (Bazylinski and Frankel, 2004; Roberts, 2015). Based on non-interacting SD behavior (Fig. 3) (Egli et al., 2010; Roberts et al., 2012), observed SD biogenic magnetite in SBB sediments in Zone 1 are likely associated with nitrate-reducing magnetotactic bacteria that occupy sharp redox gradients near the base of nitrogenous zones (e.g., near the sediment-water interface in SBB) (Bazylinski and Frankel, 2004; Kopp and Kirschvink, 2008; Roberts, 2015).

5.2. Iron mineral preservation in rapidly-accumulated reducing sediments

Although highly-reactive Fe (oxyhydr)oxides are widely preserved in most marine sediments, under sulfidic porewater conditions it is assumed that they readily dissolve and are reduced to generate Fe sulfides (Raiswell and Canfield, 2012). It has been proposed that porewater sulfide does not increase to detectable levels until highly-reactive Fe (oxyhydr)oxides are completely consumed, based on field observations at the FOAM site, Long Island Sound, Connecticut (Canfield, 1989; Canfield et al., 1992). Poulton et al. (2004) used synthetic Fe (oxyhydr)oxides and estimated reduction half lives ($t_{1/2}$) of hours (e.g., 12.3 h for ferrihydrite) to months (182 days for crystalline hematite) at pH = 7.5 and 1000 μM dissolved sulfide. Maghemite reactivity to reducing conditions was not tested in this study but should be similar to hematite according to field observations of maghemite dissolution across Fe redox boundaries (Kawamura et al., 2012; Smirnov and Tarduno, 2000). Magnetite preservation on centennial scales has previously been reported in reducing porewaters, an observation that is attributed to the smaller surface area (larger grain sizes) of natural relative to synthetic magnetite (Canfield and Berner, 1987; Canfield et al., 1992; Poulton et al., 2004). However, hematite, goethite, and maghemite all have reduction half-lives consistent with both field observations and lab experiments (Canfield and Berner, 1987; Canfield et al., 1992; Poulton et al., 2004). Thus, this Fe mineral reactivity to free sulfide scheme, though derived from synthetic minerals, should be broadly applicable to natural sediments because the synthesis techniques produce morphologically similar Fe minerals to those in natural environments (Poulton et al., 2004).

Free sulfide usually accumulates within porewaters of the upper ~5 cm of SBB sediments regardless of the sampling season (Kuwabara et al., 1999; Reimers et al., 1996), such that at ~10 cm below the SWI, porewater sulfide concentrations are typically several hundreds of μM (Komada et al., 2016; Reimers et al., 1996; Zheng et al., 2000). Additionally, Raven et al. (2016) report ~1000 μM dissolved sulfide at ~60 cm below the SWI in SBB in October 2013. Based on porewater geochemistry and a centennial age of the sediments (< 1759 CE with a ~4 mm/yr sedimentation rate) that is much longer than measured reduction half lives, any highly-reactive Fe (oxyhydr)oxides should have been rapidly converted to sulfides at sediment depths > 5 cm below the SWI. A general decreasing Fe_{dith} trend down-core suggests continual dissolution of highly-reactive Fe (oxyhydr)oxides below the top 2–3 cm where the dissolved Fe peak was observed in SBB porewaters (Kuwabara et al., 1999; Reimers et al., 1996). Yet contributions from Fe_{dith} and Fe_{ox} throughout the core suggest that highly-reactive Fe (oxyhydr)oxides are preserved on centennial timescales, corroborated

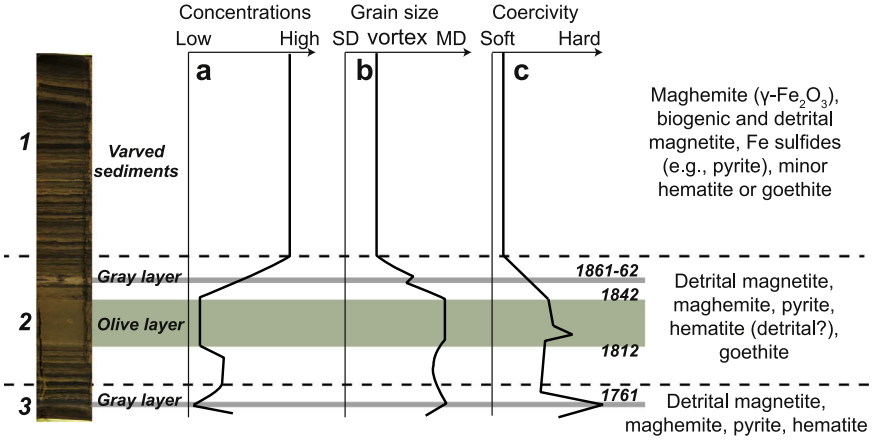

Fig. 7. Summary of down-core mineralogy from magnetic measurements in core SPR0901-04BC. As in Fig. 2, zonation (dashed lines) based on changes in magnetic mineral concentrations and concentration-independent properties is as follows: Zone 1 (0–35 cmbct), Zone 2 (35–56 cmbct) and Zone 3 (56–61 cmbct), respectively. Left, core photo of SPR0901-04BC. Right, minerals identified in each zone according to magnetic measurements. (a) Concentration profile of magnetic minerals; (b) grain size profile: SD, vortex and MD denote single-domain, vortex-state and multi-domain particles, respectively; (c) coercivity of magnetic minerals. Gray bars (1761 CE and 1861–1862 CE) represent gray layers in the core while the turbidite layer (1812–1842 CE) is shaded in dark green. (For interpretation of the references to colour in this figure legend, the reader is referred to the web version of this article.)

by magnetic analysis results (Figs. S1 and S2). Preservation of highly-reactive Fe (oxyhydr)oxides is also consistent with the results of Raven et al. (2016), where Fe_{dith} still accounts for ~1/3 of Fe_{HR} (defined as $Fe_{dith} + Fe_{py}$) at 61 cmbct. Thus, Fe_{dith} preservation in highly sulfidic porewaters below the dissolved Fe peak appears incompatible with complete/rapid reduction of Fe (oxyhydr)oxides and pyrite formation in ambient sulfidic environments.

Dissolution reaction kinetics of specific Fe minerals varies with surface area, sedimentation rates, and sulfide concentrations (Canfield and Berner, 1987; Canfield et al., 1992; Karlin, 1990a; Karlin, 1990b; Roberts and Turner, 1993). Sulfide concentrations found in SBB porewaters are similar to those used in lab experiments (Poulton et al., 2004), and thus should not be the main control of dissolution reaction kinetics. Similar morphology of synthetic and natural Fe (oxyhydr) oxides (except magnetite) makes surface area impacts less likely. In SBB, high sedimentation rates may play a role in Fe (oxyhydr)oxide preservation down-core. The sedimentation rate (~4 mm/y) in SBB is significantly higher than sedimentation rates found at other well-studied anoxic marine environments (Reimers et al., 1990; Reimers et al., 1996; Zheng et al., 2000), being ~ two orders of magnitude higher than the Black Sea sediments (0.063 mm/y, from Degens et al. (1978)), and ~4× higher than Cariaco Basin (~0.3–1 mm/y, Peterson et al. (2000)). We posit that high sedimentation rates in SBB significantly reduce the exposure of detrital minerals to sulfidic porewaters within the active diagenesis zone (several cm below the SWI), where the highest microbe-mediated sulfate reduction rates are observed and maximum Fe monosulfide formation occurs (Reimers et al., 1996). Down-core below this horizon, subsequent rapid sediment compaction lowers porosity, which hinders further reactions between porewater sulfide and sedimentary Fe (oxyhydr)oxides. Additionally, the lab experiments providing Fe oxide reduction kinetics were performed under continuously stirred conditions at 25 °C (Poulton et al., 2004), similar perhaps to the well bioturbated environment in the FOAM field experiments (Goldhaber et al., 1977). Oxic water columns in the FOAM site allow mega- and macro-fauna to bioturbate sediments despite the presence of sulfidic porewaters, which in turn reworks sediments, thereby increasing sediment-porewater interactions (e.g., irrigation fluxes of Fe (II) and sulfide) (Boudreau, 1984). This is not the case in SBB benthic environment with presence of laminations indicates the lack of bioturbation by macrofauna, which could contribute to incomplete reduction of Fe (oxyhydr)oxides in addition to the high-sedimentation rate in SBB.

5.3. The impact of water-column and porewater redox conditions on Fe speciation

Elevated Fe_T/Al ratios are typically associated with Fe sulfide formation in anoxic water columns (Lyons and Severmann, 2006). The down-core Fe_T/Al profile in SBB exhibits a consistent enrichment (Fe_T/Al of ~0.6) relative to the local lithogenic background ratio of 0.54 (except at the base of the olive layer), which suggests that anoxic bottom waters prevailed throughout the last 250 years and facilitated Fe-sulfide precipitation. Yet most downcore Fe_{HR}/Fe_T values (< 0.38) fall outside the anoxic regime. As the Fe_{HR}/Fe_T threshold value (0.38) is strictly calibrated in perennially anoxic waters, Fe_{HR}/Fe_T values in low-oxygen/oscillatory anoxic environments (inhospitable for mega- and macrofauna) are indistinguishable to those in fully-oxygenated waters, and thus Fe_{HR}/Fe_T threshold values should be applied with caution when inferring oxic/oxygenated water columns (Raiswell and Canfield, 1998; Raiswell et al., 2018). Similarly enriched Fe_T/Al associated with low Fe_{HR}/Fe_T values (< 0.38) are found in the Kau Bay, Indonesia – a water column which alternates between low-oxygen and sporadic anoxia (Middelburg, 1991). Compared to Fe_T/Al from the Kau Bay (0.87 ± 0.08) (Raiswell and Canfield, 1998), however, SBB Fe_T/Al is only weakly enriched (0.58 ± 0.03, 1SD).

Although the SBB water column is not sulfidic, significant particulate Fe enrichments ($Fe_T/Al > 0.7$) exist in the water column below sill depth (475 m) (Shiller et al., 1985). These enrichments have been attributed to mobilized Fe(II) from underlying reducing sediments, which could reprecipitate as Fe (oxyhydr)oxides in the overlying subsurface waters. Additionally, ferric hydroxo-phosphates that accumulated in coastal salt marshes could be an occasional source of Fe-rich particulates that may be transformed into Fe (oxyhydr)oxides in SBB bottom waters (Fig. 1, Shiller et al. (1985)). During regional rainfall events, ferric hydroxo-phosphates can be dispersed in surface and hyperpycnal plumes, and are subsequently transported to SBB via floc formation, particle settling, storm wave transport, gravity currents, and mass movement processes (Hendy et al., 2015; Warrick and Farnsworth, 2009a; Warrick and Farnsworth, 2009b). Under the Mediterranean climate in Southern California, Fe (oxyhydr)oxide addition via this mechanism is sporadic.

At/close to the SWI where upward diffusing sulfide fluxes have been observed, Fe-rich particulates are partially converted to Fe sulfides, which contributes to sedimentary Fe_T enrichments (Kuwabara et al., 1999; Zheng et al., 2000). Fe sulfide formation at/near the SWI is also indicated by the presence of authigenic pyrite framboids in near-surface sediments (Raven et al., 2016). Similarly, mobilized Fe addition from reducing sediments with pyrite formation at/near the SWI may have produced high Fe_T/Al in the sporadically euxinic Kau Bay (bottom water sulfide concentrations of 13 μM, Middelburg (1991)), where Fe-rich particulates in bottom waters are also reported (Middelburg et al., 1988). Mobilized Fe(II) from underlying sediments, however, is insufficient to produce significant Fe_{HR} enrichments, leading to low oxic Fe_{HR}/Fe_T values in SBB.

Fe_{py}/Fe_{HR} follows the extent of Fe_{HR} conversion to pyrite. In non-euxinic depositional environments ($Fe_{HR}/Fe_T < 0.38$), Fe_{py}/Fe_{HR} may be a proxy for sulfidic porewaters (e.g., FOAM) (Hardisty et al., 2018; Raiswell and Canfield, 1998), where complete conversion of sedimentary Fe_{HR} to pyrite leads to high Fe_{py}/Fe_{HR} ratios (> 0.7–0.8). In SBB where sulfidic porewaters prevail, the observed Fe_{py}/Fe_{HR} values are relatively low (~0.2–0.6, Figs. 5h and 6). One explanation for the low Fe_{py}/Fe_{HR} values is that pyrite oxidation during core storage converted Fe_{py} back to unsulfidized Fe_{HR}. Comparison with Raven et al. (2016) seems to suggest that Fe_{dith} in this core is not overprinted by severe pyrite oxidation to dithionite-extracted Fe (oxyhydr)oxides (Table S1, at least near the core top). We thus include an extreme scenario (high-FeS_2 scenario, Fig. 6), where we assume that all measured magnetite is formed from pyrite oxidation and therefore we remove Fe_{ox} (magnetite portion) from Fe_{HR}. Fe_{py}/Fe_{HR} calculated in this scenario represents an extreme upper limit because our magnetic analyses confirm the presence of both biogenic and lithogenic magnetite in SBB (Figs. 3 and 4). Yet, even in this high-FeS_2 scenario, low Fe_{py}/Fe_{HR} (< 0.7) persists except at the top of the turbidite layer (Fig. 5h).

Alternatively, low Fe_{py}/Fe_{HR} values could be caused by incomplete Fe_{HR} conversion to pyrite in the depositional environment. Fe (oxyhydr)oxide preservation downcore (Sections 5.1 and 5.2) indicates the sustained occurrence of unsulfidized highly-reactive Fe despite sulfide accumulation in SBB porewaters (Reimers et al., 1996) (Fig. 5). In SBB, high sedimentation rates combined with sluggish sediment-porewater interaction appear to have greatly restricted the reaction kinetics of Fe_{HR} reductive dissolution (Schimmelmann and Kastner, 1993), resulting in low Fe_{py}/Fe_{HR} values in sulfidic porewaters, at least on a centennial timescale.

5.4. Instantaneous depositional events and post-depositional diagenesis — an internal "iron shuttle" process

In addition to reaction kinetics, non-steady state diagenesis, such as the response to instantaneous sedimentary deposition events, creates another complication for Fe speciation interpretations. Two categories of instantaneous sedimentary deposition events are preserved in the SBB sedimentary record: flood-induced gray layers (e.g., the 1861 and

1761 floods) and homogenous olive layers (e.g., the turbidite triggered by the 1812 Santa Barbara earthquake) (Du et al., 2018; Hendy et al., 2015; Schimmelmann et al., 1992). Flood and turbidite layers are usually characterized by low total organic carbon (TOC), low Fe_T/Al ratios, and a concurrent Fe_{py} increase, although the magnitude of these shifts varies depending on layer thickness.

The olive turbidite layer at 43–49 cmbct provides an opportunity to observe possible post-depositional diagenetic overprinting on Fe proxies. The base of the olive layer (49 cm) contains the lowest Fe_T/Al value in the core (Fig. 5f) but the immediate overlying sample (48 cm) recovers to a typical ratio value of ~0.6. Concurrently, Fe_{py} increases within the olive layer and reaches a maximum at the top of the layer (43 cm, Fig. 5g and h) while Fe_{ace} (carbonate-bound Fe) decreases. Fe proxies suggest that the most reducing environment within the core occurred during this interval ($Fe_{HR}/Fe_T = 0.44$; ferruginous according to Fe speciation threshold values). Nevertheless, this apparent anoxic water column coincides with the basin-wide bed of *Macoma* that inhabited SBB around 1840 CE (Schimmelmann et al., 1992; Schimmelmann et al., 1990). *Macoma* spp. are a genus of bivalve intolerant of hypoxia ($O_2 < 65$ μmol/kg) such that it cannot survive typical basin conditions (Myhre et al., 2017). *Macoma* preservation in situ provides strong evidence of an unusually oxygenated benthic environment at ~1840 CE, which directly contradicts the Fe speciation interpretation. Our results suggest a "false positive" scenario where "more reducing conditions" caused by post-depositional diagenesis overprint the original oxygenated environment.

Two processes may have played a role in producing non-steady state diagenesis. Instantaneous depositional events (flood or turbidite layers) can attenuate O_2 diffusion into underlying sediments. This 'coffin-lid' effect (reduced O_2 penetration) facilitates establishment of reducing conditions in relatively organic-rich sediments immediately below the instantaneous depositional events, including Mn/Fe oxide reductive dissolution and microbial sulfate reduction (MSR) below the newly formed SWI (Anschutz et al., 2002; McKay and Pedersen, 2014; Schimmelmann, 2011). Rapid buildup of reducing conditions has been observed within weeks to months after instantaneous depositional events (Anschutz et al., 2002; Deflandre et al., 2002) and burndown is prevented for significant periods of time (McKay and Pedersen, 2014). As suggested by coercivity and S300 changes in magnetic mineral assemblages (Figs. 2h and 4), turbidite deposition introduces an external input of high-coercivity reactive Fe minerals (e.g., hematite), which are readily reduced by either microbial iron reduction (MIR), and/or ambient free sulfide (Meyers, 2007; Severmann et al., 2008).

For the newly deposited turbidite layer, porewater sulfide could come either from MSR and/or from upward sulfide diffusion out of the underlying sediments. If Fe (oxyhydr)oxide reduction outpaces sulfide production from MSR (when porewater sulfate is completely reduced) and diffusion supply, the second widely accepted process – in situ remobilization of Fe(II) from newly introduced Fe and Mn oxides – could occur (Chaillou et al., 2008; Lyons and Severmann, 2006; Meyers, 2007; Mucci et al., 2003; Raiswell et al., 2008). This process leads to diffusion and transport of Fe(II) and Mn(II), resulting in less reducing porewater conditions (i.e., the sulfide buffer of Meyers (2007)).

Complete porewater sulfate consumption has been suggested in SBB gray flood layers from $\delta^{34}S$ measurements on bulk sediments and individual pyrite aggregates. The irregular pyrite aggregates (dominant in the flood layers) have more enriched $\delta^{34}S$ values (24.2 ± 2.9‰) with respect to typical pyrite framboids ($\delta^{34}S = -24.4$‰) found in the intervening laminated sediments (Berelson et al., 2019; Bryant et al., 2019). The enriched irregular pyrite aggregates thus have a similar $\delta^{34}S$ with the original sulfate (~21‰), indicating that pyrite was formed with sulfide generated from complete sulfate reduction. In the observed SPR0901-04BC turbidite layer, a similar scenario might occur given that the sediment layer is also instantaneously deposited. Minimum Fe/Al values at the base of the olive turbidite layer (Fig. 5h) further support Fe remobilization after buffering with available sulfide. Thus, upon turbidite deposition, relative rapid responses (rapid MSR, porewater sulfate consumption, and Fe remobilization) may have contributed to development of a short-duration sulfide-free environment that enabled *Macoma* to colonize the SWI for a few years.

Fe remobilization alone is insufficient to explain the maximum Fe_{py} and Fe_{py}/Fe_{HR} at the top of the turbidite layer. Since *Macoma* spp. are intolerant of hypoxia ($O_2 < 65$ μmol/kg), and *Macoma* occupied the SWI for ~3 years (Schimmelmann et al., 1992), bottom waters must have been oxygenated long enough to allow shuttling of upward diffusing Fe(II). Although no burrowing is observed at the *Macoma* layer, the briefly oxygenated bottom waters would have allowed some macrofaunal bioturbation to facilitate Fe(II) diffusion in the porewaters. Free Fe(II) could then have been reoxidized at the top of the turbidite layer and/or repeatedly recycled near the SWI (Anderson and Raiswell, 2004; Raiswell and Anderson, 2005; Wijsman et al., 2001). Subsequent re-establishment of low-oxygen bottom water conditions could have re-initiated vigorous sulfide production near the SWI. High sedimentation rates quickly buried the turbidite layer in the following years, further contributing to sulfide accumulation in ambient porewaters. This longer-term response of porewater sulfide re-accumulation would then result in post-depositional pyrite conversion of Fe_{HR} and the Fe_{py}/Fe_{HR} peak at the upper boundary of the turbidite layer. This internal "shuttle-like" mechanism involves the reduction of fresh Fe (oxyhydr)oxides introduced by the turbidite layer that produces a local Fe_T/Al depletion, the upward diffusion and oxidation of Fe(II), and finally re-precipitation as pyrite when sulfidic porewaters re-established during the years following turbidite deposition. A further possibility is that *Macoma* spp., freshly suffocated by low-oxygen bottom water, may have provided extra highly-reactive organic carbon contributing to reductive dissolution of Fe (oxyhydr)oxides and pyrite conversion at the top of the turbidite layer (Emiroğlu et al., 2004). Yet, the *Macoma* layer coincides with lower than average TOC values (Wang et al., 2017).

While intense Fe(II) migration in the other two much-thinner flood layers is not evident in the Fe speciation results (except slight Fe_T/Al reduction), these layers contain similar pyrite peaks and local Fe_{py}/Fe_{HR} maxima. The flood sediments also rapidly deposit a new source of Fe_{HR} as demonstrated by L-ratios (Fig. 4), therefore, Fe(II) mobilization and sulfide buffering should occur similar to the 1812 turbidite, followed by pyrite conversion in the ambient sulfidic porewaters. Different slopes on the L-ratio vs. HIRM plot (Fig. 4) demonstrate that the 1761 flood layer contains a magnetically harder mineral assemblage (e.g., higher-coercivity hematite) than the turbidite layer. Subtle differences in iron mineral assemblages are likely in each turbidite and flood layer due to sediment source variations (downslope submarine landslides relative to different river catchment contributions). Thus, instantaneous depositional events can perturb porewater redox conditions that control later diagenetic processes, initiating non-steady state diagenesis and erasing the original redox record. This post-depositional non-steady state diagenesis likely significantly altered the steady-state redox signal in Fe proxies, leading to "false positive" anoxic interpretations. Given widespread occurrence of instantaneous depositional events in the geological record (e.g., turbidites triggered by submarine landslides, storms, etc.), care should be taken when interpreting diagenetic redox environments.

5.5. Trace metal enrichments in the Santa Barbara Basin

To further understand porewater redox chemistry and Fe enrichments, trace metal enrichments (Wang et al., 2017) are compared with Fe speciation results from the same samples. Manganese is consistently depleted in the core; its relatively constant low enrichment factor (~0.4) indicates that porewaters were always sufficiently reducing to remobilize Mn (Table S3). Rhenium and U enrichments behave similarly as expected ($r = 0.6384$, $p < 0.0001$), given the typically low-oxygen bottom water in the central SBB (Fig. 8). Molybdenum enrichments are not correlated with Fe_{HR}/Fe_T ($r = -0.1695$, $p = 0.2076$) and

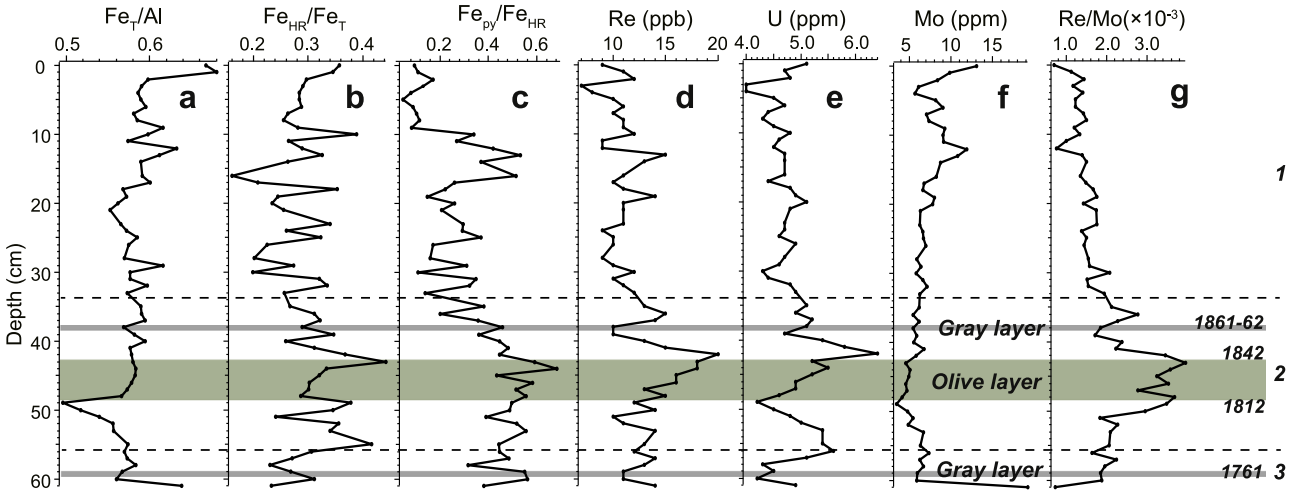

Fig. 8. Down-core comparison of iron redox proxies and trace metals in SPR0901-04BC. (a) Fe_T/Al; (b) Fe_{HR}/Fe_T; (c) Fe_{py}/Fe_{HR}; (d) Rhenium (ppb); (e) Uranium (ppm); (f) Molybenum (ppm); (g) Re/Mo ratios ($\times 10^{-3}$). Zonation (dashed lines) based on changes in magnetic mineral concentrations and concentration-independent properties is as follows: Zone 1 (0–35 cmbct), Zone 2 (35–56 cmbct) and Zone 3 (56–61 cmbct), respectively. Gray bars (1761 CE and 1861–1862 CE) represent gray layers in the core while the turbidite layer (1812–1842 CE) is shaded in dark green. (For interpretation of the references to colour in this figure legend, the reader is referred to the web version of this article.)

are negatively correlated to Fe_{py}/Fe_{HR} ($r = -0.2821$, $p < 0.05$), indicating disagreement between the two euxinic indicators. In contrast to Fe_{py} and Fe_{py}/Fe_{HR}, the enrichment factor of Mo (Mo_{EF}) reaches its minimum within the turbidite-triggered olive layer, where Mo is close to or slightly depleted with respect to the lithogenic background, consistent with well-oxygenated bottom water as indicated by the presence of *Macoma* (Tables S2 and S3). Mo has been shown to precipitate near the SWI in SBB (Zheng et al., 2000), and thus this metal should record the original bottom-water redox chemistry in the basin (Wang et al., 2017).

Molybdenum enrichment in sediments is controlled by enhanced Mo delivery via particulate shuttles (i.e., Fe-Mn shuttle effects), changes in water-column trace metal concentrations, and bottom water redox conditions (Algeo and Tribovillard, 2009; Cheng et al., 2016; Tribovillard et al., 2012). In the particulate shuttle process, Mo is readily adsorbed onto Fe-Mn oxides, thus precipitation and reduction of Fe-Mn oxides could strongly accelerate Mo delivery to sediments (Algeo and Tribovillard, 2009; Tribovillard et al., 2012). Uranium affinity with Fe-Mn oxides, however, is much more limited, and thus an efficient Fe-Mn shuttle could result in a higher Mo_{EF} than would be expected from euxinic water columns (e.g., Cariaco Basin, Tribovillard et al. (2012)). Variations in water-column trace metal concentrations can impact enrichment in sediments. This occurs in the Black Sea where Mo is depleted in the water column and as a result Black Sea sediments have lower than expected Mo_{EF} (Algeo and Tribovillard, 2009). Finally, Mo precipitation is suggested to be initiated at a H_2S threshold of ~0.1 μM at the SWI (Zheng et al., 2000), but a threshold of 11 μM is required for MoO_4^{2-} to abruptly switch to MoS_4^{2-} (Erickson and Helz, 2000). Given the typically low sulfide concentration near the SWI in SBB, partial conversion to intermediate thiomolybdate phases ($MoO_xS_{4-x}^{2-}$) is expected (Cheng et al., 2016; Erickson and Helz, 2000; Helz et al., 1996).

The cross-plot of Mo_{EF} vs. U_{EF} provides insights into the contribution of the three processes in the SBB (Fig. 9, Algeo and Tribovillard (2009); Cheng et al. (2016)). Molybdenum and U enrichment factors mostly fall between 0.1 × SW (seawater value of Mo:U weight ratio for present Pacific seawater is ~3.2; Tribovillard et al. (2012)) and 0.3 × SW, consistent with prevailing low-oxygen water columns. However, Fe and Mn particulate shuttle effects are not observed in the cross-plot (Fig. 9), which suggests that particulate shuttles only have, if any, minor impacts on Mo precipitation in SBB sediments. Additionally, Zheng et al. (2000) reported gradually depleted porewater Mo below

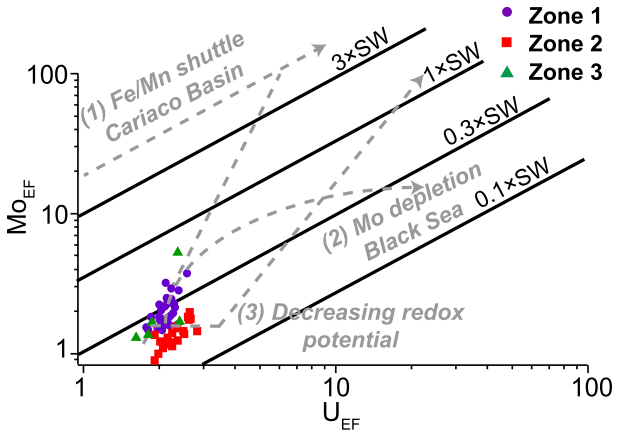

Fig. 9. Cross-plot of Mo_{EF} vs. U_{EF} in core SPR0901-04BC. Purple circles (Zone 1: 0–35 cmbct), red squares (Zone 2: 35–56 cmbct), and green triangles (Zone 3: 56–61 cmbct), respectively, represent enrichment factors (EF) for samples from the three magnetic mineral zones. Diagonal solid lines represent multiples (0.3, 1, and 3) of SW (seawater) lines in the modern seawater (average weight ratio of Mo:U of ~3.2). Gray dashed lines highlight general patterns of U_{EF} and Mo_{EF} in the unrestricted marine environment, Black Sea (Mo depletion in the water column) and Cariaco Basin ("particulate shuttle" trend) modified from Tribovillard et al. (2012). (For interpretation of the references to colour in this figure legend, the reader is referred to the web version of this article.)

5 cm depth, which suggests that there is not a significant amount of post-depositional release of Mo from Fe-Mn oxides. Molybdenum depletion in the SBB water column has not been observed (Zheng et al., 2000), and thus trace metal precipitation in the basin should be primarily related to porewater redox chemistry and/or vigorous redox reactions at the SWI. Thus, trace metal enrichments in the SBB contain a primary signal that provides information on water-column redox conditions at the time of deposition, while the primary Fe enrichment signal is overprinted by post-depositional non-steady state diagenesis.

6. Conclusions and implications

Sedimentary redox-sensitive metal responses to redox conditions are assumed to be directly linked to the overlying water column. Under certain circumstances, this linkage can be compromised because redox

conditions are also closely associated with ambient porewater chemistry. The geochemical setting of the Santa Barbara Basin (SBB), California – a weakly-silled, high productivity basin overlain by low-oxygen bottom waters and containing sulfidic porewaters – represents an intermediate environment between oxic and euxinic water columns. Geochemistry/magnetism records from the box core SPR0901-04BC provide a centennial-scale snapshot on how Fe speciation results can be obscured by high sedimentation rates and post-depositional diagenesis, with more diagenetic processes likely affecting the down-core Fe mineralogy on longer time scales. Unlike the Cariaco Basin or the Black Sea where euxinia is observed in the water column (Algeo and Rowe, 2012; Lyons and Severmann, 2006; Raiswell and Anderson, 2005), only porewaters in SBB are sulfidic and the redoxcline (oxic versus anoxic) is at or close to the sediment water interface (SWI). In SBB, vigorous redox reactions occur near the SWI; therefore, enrichments of redox sensitive metals should reflect water column dissolved oxygen (Reimers et al., 1996; Zheng et al., 2000).

Mineralogical shifts related to local geochemistry and diagenesis in SBB sediments can be observed by combining magnetic measurements with iron speciation. Fe_T/Al indicates a sustained anoxic depositional environment (except at the base of the turbidite layer) due to enrichment by authigenic Fe sulfide formation at or close to the SWI. Our results also demonstrate that biogenic magnetite can be temporarily preserved in sulfidic porewaters and there are frequent instances of highly-reactive Fe (oxyhydr)oxides escaping reduction, at least on decadal to centennial time scales. We suggest that highly-reactive Fe reduction kinetics could be inhibited by the high sedimentation rates and minimal bioturbation, which reduce sediment-porewater interactions and prevent complete/rapid pyrite conversion in porewaters. Caution should, therefore, be taken when using Fe_{py}/Fe_{HR} as a sulfidic porewater proxy in recently deposited sediments (Hardisty et al., 2018); mineralogy should be checked for complete/rapid pyrite conversion. In addition, non-steady state diagenesis following instantaneous sediment depositional events perturbs the geochemistry of the depositional environment, notably through the increased supply of fresh highly-reactive Fe that results in sulfide buffering. Within the 1812 turbidite layer, recently introduced reactive Fe (oxyhydr)oxides buffered upward diffusing free sulfide from underlying sediments and were reduced to Fe (II) that subsequently diffused upward in porewaters. In the SBB, this turbidite deposition created a less reducing (sulfide free) benthic environment that allowed a brief ~3 year colonization of the bivalve, *Macoma* spp. With the greater availability of shuttled Fe, subsequent re-establishment of sulfidic porewater resulted in rapid pyrite precipitation and thus led to a "false positive" (more reducing conditions) in Fe speciation results, overprinting the original oxygenated bottom water responses. Trace metal (Mo, Re, and U) precipitation in SBB appears to be primarily controlled by reducing conditions at the SWI and is not overprinted by down-core diagenesis.

Instantaneous depositional events such as turbidites are common in marginal marine sedimentary environments (Hensen et al., 2003; Otero et al., 2003; Robinson and Sahota, 2000; Robinson et al., 2000; Yücel et al., 2010), and yet are rarely considered in geochemical redox reconstructions of past marine environments. Frequent instantaneous depositional events in SBB, in addition to low-oxygen water conditions and the centennial scale of the record, make Fe speciation a poor proxy choice for local redox reconstructions. Trace metals, however, preserve original redox shifts in the bottom waters of the basin. Despite observed complications in this centennial-scale reconstruction, Fe speciation still deserves some consideration and may provide valuable information on deep-time redox history.

Supplementary data to this article can be found online at https://doi.org/10.1016/j.chemgeo.2019.04.018.

Acknowledgements

This work is supported by the National Science Foundation (grant number NSF OCE-1304327) awarded to I.H., the Scott Turner Award to Y.W., and by the Rackham Graduate School of the University of Michigan. Part of this work was performed as a US Visiting Student Fellow at the Institute for Rock Magnetism (IRM) at the University of Minnesota. The IRM is a US National Multi-user Facility supported through the Instrumentation and Facilities program of the National Science Foundation, Earth Sciences Division, and by funding from the University of Minnesota. We thank Mike Jackson and Peter Solheid for thoughtful discussions and technical support at the IRM. This is IRM publication 1708. We acknowledge Arndt Schimmelmann for helpful discussions. We appreciate comments from Andrew P. Roberts and other two anonymous reviewers, which greatly improved this manuscript. All geochemical data can be accessed from the Supplementary Information.

References

Algeo, T.J., Rowe, H., 2012. Paleoceanographic applications of trace-metal concentration data. Chem. Geol. 324-325 (2012), 6–18.
Algeo, T.J., Tribovillard, N., 2009. Environmental analysis of paleoceanographic systems based on molybdenum–uranium covariation. Chem. Geol. 268 (3–4), 211–225.
Anderson, T.F., Raiswell, R., 2004. Sources and mechanism for the enrichment of highly reactive iron in euxinic Black Sea sediments. Am. J. Sci. 304, 203–233.
Anschutz, P., Jorissen, F.J., Chaillou, G., Abu-Zied, R., Fontanier, C., 2002. Recent turbidite deposition in the eastern Atlantic: early diagenesis and biotic recovery. J. Mar. Res. 60, 835–854.
Bazylinski, D.A., Frankel, R.B., 2004. Magnetosome formation in prokaryotes. Nat. Rev. Microbiol. 2, 217.
Berelson, W.M., et al., 2005. Anaerobic diagenesis of silica and carbon in continental margin sediments: discrete zones of TCO2 production. Geochim. Cosmochim. Acta 69 (19), 4611–4629.
Berelson, W.M., et al., 2019. Santa Barbara Basin flood layers: impact on sediment diagenesis. In: From the Mountains to the Abyss: The California Borderland as an Archive of Southern California Geologic Evolution. vol. 110 Society for Sedimentary Geology.
Berner, R.A., 1981. A new geochemical classification of sedimentary environments. J. Sediment. Petrol. 51 (2), 359–365.
Boudreau, B.P., 1984. On the equivalence of nonlocal and radial-diffusion models for porewater irrigation. J. Mar. Res. 42 (3), 731–735.
Bryant, R.N., et al., 2019. Sulfur isotope analysis of microcrystalline iron sulfides using secondary ion mass spectrometry imaging: extracting local paleo-environmental information from modern and ancient sediments. Rapid Commun. Mass Spectrom. 33 (5), 491–502.
Calvert, S.E., Pedersen, T., 1996. Sedimentary geochemistry of manganese - implications for the environment of formation of manganiferous black shales. Econ. Geol. 91, 26–47.
Calvert, S.E., Pedersen, T.F., 2007. Elemental Proxies for Palaeoclimatic and Palaeoceanographic Variability in Marine Sediments: Interpretation and Application, Developments in Marine Geology. pp. 567–644.
Canfield, D.E., 1989. Reactive iron in marine sediments. Geochim. Cosmochim. Acta 53 (3), 619–632.
Canfield, D.E., Berner, R.A., 1987. Dissolution and pyritization of magnetite in anoxic marine sediments. Geochim. Cosmochim. Acta 51 (3), 645–659.
Canfield, D.E., Raiswell, R., Westrich, J.T., Reaves, C.M., Berner, R.A., 1986. The use of chromium reduction in the anlysis of reduced inorganic sulfur in sediments and shales. Chem. Geol. 54 (1986), 149–155.
Canfield, D.E., Raiswell, R., Bottrell, S., 1992. The reactivity of sedimentary iron minerals toward sulfide. Am. J. Sci. 292 (9), 659–683.
Canfield, D.E., Poulton, S.W., Narbonne, G.M., 2007. Late-Neoproterozoic deep-ocean oxygenation and the rise of animal life. Science 315 (5808), 92–94.
Carvallo, C., Özdemir, Ö., Dunlop, D.J., 2004. First-order reversal curve (FORC) diagrams of elongated single-domain grains at high and low temperatures. J. Geophys. Res. Solid Earth 109 (B4).
Chaillou, G., Schäfer, J., Blanc, G., Anschutz, P., 2008. Mobility of Mo, U, As, and Sb within modern turbidites. Mar. Geol. 254 (3–4), 171–179.
Chang, S.-B.R., Kirschvink, J.L., 1989. Magnetofossils, the magnetization of sediments and the evolution of magnetite biomineralization. Annu. Rev. Earth Planet. Sci. 17, 169–195.
Chang, L., et al., 2009. Low-temperature magnetic properties of greigite (Fe3S4). Geochem. Geophys. Geosyst. 10 (1).
Chang, L., et al., 2013. Low-temperature magnetic properties of pelagic carbonates: oxidation of biogenic magnetite and identification of magnetosome chains. J. Geophys. Res. Solid Earth 118, 6049–6065.
Chang, L., Heslop, D., Roberts, A.P., Rey, D., Mohamed, K.J., 2016a. Discrimination of biogenic and detrital magnetite through a double Verwey transition temperature. J. Geophys. Res. Solid Earth 121, 3–14.
Chang, L., et al., 2016b. Widespread occurrence of silicate-hosted magnetic mineral inclusions in marine sediments and their contribution to paleomagnetic recording. J. Geophys. Res. Solid Earth 121, 8415–8431.
Cheng, M., et al., 2016. Marine Mo biogeochemistry in the context of dynamically euxinic

mid-depth waters: a case study of the lower Cambrian Niutitang shales, South China. Geochim. Cosmochim. Acta 183, 79–93.
Clarkson, M.O., Poulton, S.W., Guilbaud, R., Wood, R.A., 2014. Assessing the utility of Fe/Al and Fe-speciation to record water column redox conditions in carbonate-rich sediments. Chem. Geol. 382, 111–122.
Crusius, J., Thomson, J., 2000. Comparative behavior of authigenic Re, U, and Mo during reoxidation and subsequent long-term burial in marine sediments. Geochim. Cosmochim. Acta 64 (13), 2233–2242.
Crusius, J., Calvert, S., Pedersen, T., Sage, D., 1996. Rhenium and molybdenum enrichments in sediments as indicators of oxic, suboxic and sulfidic conditions of deposition. Earth Planet. Sci. Lett. 145, 65–78.
Day, R., Fuller, M., Schmidt, V.A., 1977. Hysteresis properties of titanomagnetites: Grain-size and compositional dependence. Phys. Earth Planet. Inter. 13, 260–267.
Deflandre, B., Mucci, A., Gagné, J.-P., Guignard, C., Sundby, B., 2002. Early diagenetic processes in coastal marine sediments disturbed by a catastrophic sedimentation event. Geochim. Cosmochim. Acta 66 (14), 2547–2558.
Degens, E.T., Stoffers, P., Golubic, S., Dickman, M.D., 1978. Varve chronology: estimated rates of sedimentation in the Black Sea deep basin. pp. 499–508.
Dekkers, M.J., 1989a. Magnetic properties of natural goethite—II. TRM behaviour during thermal and alternating field demagnetization and low-temperature treatment. Geophys. J. Int. 97 (2), 341–355.
Dekkers, M.J., 1989b. Magnetic properties of natural pyrrhotite. II. High- and low-temperature behaviour of Jrs and TRM as function of grain size. Phys. Earth Planet. Inter. 57, 266–283.
Du, X., Hendy, I., Schimmelmann, A., 2018. A 9000-year flood history for Southern California: a revised stratigraphy of varved sediments in Santa Barbara Basin. Mar. Geol. 397, 29–42.
Dunlop, D.J., 2002. Theory and application of the day plot (M_{rs}/M_s versus H_{cr}/H_c) 1. Theoretical curves and tests using titanomagnetite data. J. Geophys. Res. 107 (B3).
Egli, R., 2013. VARIFORC: an optimized protocol for calculating non-regular first-order reversal curve (FORC) diagrams. Glob. Planet. Chang. 110, 302–320.
Egli, R., Chen, A.P., Winklhofer, M., Kodama, K.P., Horng, C.-S., 2010. Detection of noninteracting single domain particles using first-order reversal curve diagrams. Geochem. Geophys. Geosyst. 11 (1), 1–22.
Emiroğlu, S., Rey, D., Petersen, N., 2004. Magnetic properties of sediment in the Ría de Arousa (Spain): dissolution of iron oxides and formation of iron sulphides. Phys. Chem. Earth, Parts A/B/C 29 (13-14), 947–959.
Erickson, B.E., Helz, G.R., 2000. Molybdenum(VI) speciation in sulfidic waters: stability and lability of thiomolybdates. Geochim. Cosmochim. Acta 64 (7), 1149–1158.
Frederichs, T., von Dobeneck, T., Bleil, U., Dekkers, M.J., 2003. Towards the identification of siderite, rhodochrosite, and vivianite in sediments by their low-temperature magnetic properties. Phys. Chem. Earth 28, 669–679.
Goldhaber, M.B., et al., 1977. Sulfate reduction, diffusion, and bioturbation in Long Island Sound sediments; report of the FOAM Group. Am. J. Sci. 277 (3), 193–237.
Hardisty, D.S., et al., 2018. An evaluation of sedimentary molybdenum and iron as proxies for pore fluid paleoredox conditions. Am. J. Sci. 318 (5), 527–556.
Harrison, R.J., Feinberg, J.M., 2008. An improved algorithm for calculating first-order-reversal curve distributions using locally weighted regression smoothing. Geochem. Geophys. Geosyst. 9 (5), 1–11.
Harrison, R.J., Lascu, I., 2014. FORCulator: a micromagnetic tool for simulating first-order reversal curve diagrams. Geochem. Geophys. Geosyst. 15 (12), 4671–4691.
Harrison, B.K., Zhang, H., Berelson, W., Orphan, V.J., 2009. Variations in archaeal and bacterial diversity associated with the sulfate-methane transition zone in continental margin sediments (Santa Barbara Basin, California). Appl. Environ. Microbiol. 75 (6), 1487–1499.
Helz, G.R., Dolor, M.K., 2012. What regulates rhenium deposition in euxinic basins? Chem. Geol. 304-305, 131–141.
Helz, G.R., et al., 1996. Mechanism of molybdenum removal from the sea and its concentration in black shales: EXAFS evidence. Geochim. Cosmochim. Acta 60 (19), 3631–3642.
Helz, G.R., Bura-Nakić, E., Mikac, N., Ciglenečki, I., 2011. New model for molybdenum behavior in euxinic waters. Chem. Geol. 284 (3–4), 323–332.
Hendy, I.L., Pedersen, T.F., 2005. Is pore water oxygen content decoupled from productivity on the California margin? Trace element results from Ocean Drilling Program Hole 1017E, San Lucia slope, California. Paleoceanography 20 (4), 1–12.
Hendy, I.L., Napier, T.J., Schimmelmann, A., 2015. From extreme rainfall to drought: 250 years of annually resolved sediment deposition in Santa Barbara Basin, California. Quat. Int. 387, 3–12.
Hensen, C., et al., 2003. Control of sulfate pore-water profiles by sedimentary events and the significance of anaerobic oxidation of methane for the burial of sulfur in marine sediments. Geochim. Cosmochim. Acta 67 (14), 2631–2647.
Horng, C.-S., Roberts, A.P., 2018. The low-temperature Besnus magnetic transition: signals due to monoclinic and hexagonal pyrrhotite. Geochem. Geophys. Geosyst. 19 (9), 3364–3375.
Hunt, C.P., Moskowitz, B.M., Banerjee, S.K., 1995. Magnetic properties of rocks and minerals. In: Ahrens, T.J. (Ed.), Rock Physics & Phase Relations: A Handbook of Physical Constants. American Geophysical Union, Washington, D. C, pp. 189–204.
Jackson, M., Solheid, P., 2010. On the quantitative analysis and evaluation of magnetic hysteresis data. Geochem. Geophys. Geosyst. (Q04Z15), 11.
Kaplan, I.R., Emery, K.O., Rittenberg, S.C., 1963. The distribution and isotopic abundance of sulphur in recent marine sediments off southern California. Geochim. Cosmochim. Acta 27 (4), 297–331.
Karlin, R., 1990a. Magnetic mineral diagenesis in suboxic sediments at Bettis Site W-N, NE Pacific Ocean. J. Geophys. Res. Solid Earth 95 (B4), 4421–4436.
Karlin, R., 1990b. Magnetite diagenesis in marine sediments from the Oregon continental margin. J. Geophys. Res. Solid Earth 95 (B4), 4405–4419.
Kawamura, N., Ishikawa, N., Torii, M., 2012. Diagenetic alteration of magnetic minerals in Labrador Seasediments (IODP Sites U1305, U1306, and U1307). Geochem. Geophys. Geosyst. 13 (8), 1–16.
Komada, T., et al., 2016. Organic matter cycling across the sulfate-methane transition zone of the Santa Barbara Basin, California Borderland. Geochim. Cosmochim. Acta 176, 259–278.
Kopp, R.E., Kirschvink, J.L., 2008. The identification and biogeochemical interpretation of fossil magnetotactic bacteria. Earth Sci. Rev. 86 (1–4), 42–61.
Kuwabara, J.S., Geen, A.V., Mccorkle, D.C., Bernhard, J.M., 1999. Dissolved sulfide distributions in the water column and sediment pore waters of the Santa Barbara Basin. Geochim. Cosmochim. Acta 63 (15), 2199–2209.
Leslie, B.W., Hammond, D.E., Berelson, W.M., Lund, S.P., 1990. Diagenesis in anoxic sediments from the California continental borderland and its influence on iron, sulfur, and magnetite behavior. J. Geophys. Res. 95 (B4), 4453.
Li, C., et al., 2010. A stratified redox model for the Ediacaran ocean. Science 328 (5974), 80–83.
Li, C., et al., 2015. Marine redox conditions in the middle Proterozoic Ocean and isotopic constraints on authigenic carbonate formation- Insights from the Chuanlinggou Formation, Yanshan Basin, North China. Geochim. Cosmochim. Acta 150 (2015), 90–105.
Liu, Q., et al., 2006. Characteristic low-temperature magnetic properties of aluminous goethite [α-(Fe, Al)OOH] explained. J. Geophys. Res. Solid Earth 111 (B12).
Liu, Q., Roberts, A.P., Torrent, J., Horng, C.-S., Larrasoaña, J.C., 2007. What do the HIRM and S-ratio really measure in environmental magnetism? Geochem. Geophys. Geosyst. 8 (9), 1–10.
Liu, Q., et al., 2012. Environmental magnetism: principles and applications. Rev. Geophys. 50 (4).
Lyons, T.W., Severmann, S., 2006. A critical look at iron paleoredox proxies: new insights from modern euxinic marine basins. Geochim. Cosmochim. Acta 70 (23), 5698–5722.
Lyons, T.W., Reinhard, C.T., Planavsky, N.J., 2014. The rise of oxygen in Earth's early ocean and atmosphere. Nature 506 (7488), 307–315.
Madison, A.S., Tebo, B.M., Mucci, A., Sundby, B., Luther, G.W.I., 2013. Abundant porewater Mn(III) is a major component of the sedimentary redox system. Science 341 (6148), 875–878.
März, C., Hoffmann, J., Bleil, U., de Lange, G.J., Kasten, S., 2008a. Diagenetic changes of magnetic and geochemical signals by anaerobic methane oxidation in sediments of the Zambezi deep-sea fan (SW Indian Ocean). Mar. Geol. 255 (3–4), 118–130.
März, C., et al., 2008b. Redox sensitivity of P cycling during marine black shale formation- dynamics of sulfidic and anoxic, non-sulfidic bottom waters. Geochim. Cosmochim. Acta 72 (2008), 3703–3717.
McKay, J.L., Pedersen, T.F., 2014. Geochemical response to pulsed sedimentation: implications for the use of Mo as a paleo-proxy. Chem. Geol. 382, 83–94.
McKay, J., Pedersen, T., Mucci, A., 2007. Sedimentary redox conditions in continental margin sediments (N.E. Pacific) — influence on the accumulation of redox-sensitive trace metals. Chem. Geol. 238 (3–4), 180–196.
McManus, J., Berelson, W.M., Klinkhammer, G.P., Hammond, D.E., Holm, C., 2005. Authigenic uranium: relationship to oxygen penetration depth and organic carbon rain. Geochim. Cosmochim. Acta 69 (1), 95–108.
McManus, J., et al., 2006. Molybdenum and uranium geochemistry in continental margin sediments: paleoproxy potential. Geochim. Cosmochim. Acta 70 (18), 4643–4662.
Meyers, S.R., 2007. Production and preservation of organic matter: the significance of iron. Paleoceanography 22 (4), 1–16.
Middelburg, J.J., 1991. Organic carbon, sulphur, and iron in recent semi-euxinic sediments of Kau Bay, Indonesia. Geochim. Cosmochim. Acta 55 (3), 815–828.
Middelburg, J.J., De Lange, G.J., Van Der Sloot, H.A., Van Emburg, P.R., Sophiah, S., 1988. Particulate manganese and iron framboids in Kau Bay, Halmahera (eastern Indonesia). Mar. Chem. 23 (3), 353–364.
Morford, J.L., Emerson, S.R., 1999. The geochemistry of redox sensitive trace metals in sediments. Geochim. Cosmochim. Acta, 63(11/12): 1735–1750.
Mucci, A., 2004. The behavior of mixed Ca–Mn carbonates in water and seawater: controls of manganese concentrations in marine porewaters. Aquat. Geochem. 10 (1–2), 139–169.
Mucci, A., Boudreau, B., Guignard, C., 2003. Diagenetic mobility of trace elements in sediments covered by a flash flood deposit: Mn, Fe and As. Appl. Geochem. 18 (7), 1011–1026.
Myhre, S.E., Kroeker, K.J., Hill, T.M., Roopnarine, P., Kennett, J.P., 2017. Community benthic paleoecology from high-resolution climate records: mollusca and foraminifera in post-glacial environments of the California margin. Quat. Sci. Rev. 155, 179–197.
Otero, X.L., Huerta-Diaz, M.A., Macías, F., 2003. Influence of a turbidite deposit on the extent of pyritization of iron, manganese and trace metals in sediments from the Guaymas Basin, Gulf of California (Mexico). Appl. Geochem. 18 (8), 1149–1163.
Özdemir, Ö., Banerjee, S.K., 1984. High temperature stability of maghemite (γ-Fe2O3). Geophys. Res. Lett. 11 (3), 161–164.
Özdemir, Ö., Dunlop, D.J., 1996. Thermoremanence and Néel temperature of goethite. Geophys. Res. Lett. 23 (9), 921–924.
Özdemir, Ö., Dunlop, D.J., 2010. Hallmarks of maghemitization in low-temperature remanence cycling of partially oxidized magnetite nanoparticles. J. Geophys. Res. 115 (B02101).
Passier, H.F., Dekkers, M.J., de Lange, G.J., 2001. Magnetic properties and geochemistry of the active oxidation front and the youngest sapropel in the eastern Mediterranean Sea. Geophys. J. Int. 145 (3), 604–614.
Peterson, L.C., et al., 2000. Late Quaternary Stratigraphy and Sedimentation at Site 1002, Cariaco Basin (Venezuela).
Pike, C.R., Roberts, A.P., Verosub, K.L., 1999. Characterizing interactions in fine magnetic particle systems using first order reversal curves. J. Appl. Phys. 85 (9), 6660–6667.

Poulton, S.W., Canfield, D.E., 2005. Development of a sequential extraction procedure for iron: implications for iron partitioning in continentally derived particulates. Chem. Geol. 214 (3–4), 209–221.
Poulton, S.W., Canfield, D.E., 2011. Ferruginous conditions: a dominant feature of the ocean through Earth's history. Elements 7, 107–112.
Poulton, S.W., Raiswell, R., 2002. The low-temperature geochemical cycle of iron: from continental fluxes to marine sediment deposition. Am. J. Sci. 302 (9), 774–805.
Poulton, S.W., Raiswell, R., 2005. Chemical and physical characteristics of iron oxides in riverine and glacial meltwater sediments. Chem. Geol. 218 (3–4), 203–221.
Poulton, S.W., Krom, M.D., Raiswell, R., 2004. A revised scheme for the reactivity of iron (oxyhydr)oxide minerals towards dissolved sulfide. Geochim. Cosmochim. Acta 68 (18), 3703–3715.
Poulton, S.W., et al., 2015. A continental-weathering control on orbitally driven redox-nutrient cycling during Cretaceous Oceanic Anoxic Event 2. Geology 43 (11), 963–966.
Raiswell, R., Anderson, T.F., 2005. Reactive iron enrichment in sediments deposited beneath euxinic bottom waters: constraints on supply by shelf recycling. In: McDonald, I., Boyce, A.J., Butler, I.B., Herrington, R.J., Polya, D.A. (Eds.), Mineral Deposits and Earth Evolution. Geological Society of London, London, pp. 179–194.
Raiswell, R., Canfield, D.E., 1998. Sources of iron for pyrite formation in marine sediments. Am. J. Sci. 298 (3), 219–245.
Raiswell, R., Canfield, D.E., 2012. Geochemical Perspectives: The Iron Biogeochemical Cycle Past and Present. vol. 1.
Raiswell, R., et al., 2008. Turbidite depositional influences on the diagenesis of Beecher's Trilobite Bed and the Hunsrück Slate; sites of soft tissue pyritization. Am. J. Sci. 308 (2), 105–129.
Raiswell, R., et al., 2018. The iron paleoredox proxies: a guide to the pitfalls, problems and proper practice. Am. J. Sci. 318, 491–526.
Raven, M.R., Sessions, A.L., Fischer, W.W., Adkins, J.F., 2016. Sedimentary pyrite δ34S differs from porewater sulfide in Santa Barbara Basin: proposed role of organic sulfur. Geochim. Cosmochim. Acta 186, 120–134.
Reimers, C.E., Lange, C., Tabak, M., Bernhard, J., 1990. Seasonal spillover and varve formation in the Santa Barbara Basin, California. Limnol. Oceanogr. 35 (7), 1577–1585.
Reimers, C.E., Ruttenberg, K.C., Canfield, D.E., Christiansen, M.B., Martin, J.B., 1996. Porewater pH and authigenic phases formed in the uppermost sediments of Santa Barbara Basin. Geochim. Cosmochim. Acta 60 (21), 4037–4057.
Reinhard, C.T., Raiswell, R., Scott, C., Anbar, A.D., Lyons, T.W., 2009. A late Archean sulfidic sea stimulated by early oxidative weathering of the continents. Science 326 (5953), 713–716.
Rickard, D., Morse, J.W., 2005. Acid volatile sulfide (AVS). Mar. Chem. 97 (3–4), 141–197.
Roberts, A.P., 2015. Magnetic mineral diagenesis. Earth Sci. Rev. 151 (2015), 1–47.
Roberts, A.P., Turner, G.M., 1993. Diagenetic formation of ferrimagnetic iron sulphide minerals in rapidly deposited marine sediments, South Island, New Zealand. Earth Planet. Sci. Lett. 115, 257–273.
Roberts, A.P., Pike, C.R., Verosub, K.L., 2000. First-order reversal curve diagrams: a new tool for characterizing the magnetic properties of natural samples. J. Geophys. Res. 105 (B12), 28461–28475.
Roberts, A.P., et al., 2006. Characterization of hematite (α-Fe_2O_3), goethite (α-FeOOH), greigite (Fe_3S_4), and pyrrhotite (Fe_7S_8) using first-order reversal curve diagrams. J. Geophys. Res. 111 (B12).
Roberts, A.P., Chang, L., Rowan, C.J., Horng, C.-S., Florindo, F., 2011. Magnetic properties of sedimentary greigite (Fe3S4): an update. Rev. Geophys. 49 (1).
Roberts, A.P., Chang, L., Heslop, D., Florindo, F., Larrasoaña, J.C., 2012. Searching for single domain magnetite in the "pseudo-single-domain" sedimentary haystack: implications of biogenic magnetitepreservation for sediment magnetism and relative paleointensity determinations. J. Geophys. Res. (B08104), 117.
Roberts, A.P., Heslop, D., Zhao, X., Pike, C.R., 2014. Understanding fine magnetic particle systems through use of first-order reversal curve diagrams. Rev. Geophys. 52, 557–602.
Roberts, A.P., et al., 2017. Resolving the origin of pseudo-single domain magnetic behavior. J. Geophys. Res. Solid Earth 122 (12), 9534–9558.
Roberts, A.P., Tauxe, L., Heslop, D., Zhao, X., Jiang, Z., 2018. A critical appraisal of the "Day" diagram. J. Geophys. Res. Solid Earth 123, 2618–2644.
Robinson, S.G., Sahota, J.T.S., 2000. Rock-magnetic characterization of early, redoxomorphic diagenesis in turbiditic sediments from the Madeira Abyssal Plain. Sedimentology 47 (2), 367–394.
Robinson, S.G., Sahota, J.T.S., Oldfield, F., 2000. Early diagenesis in North Atlantic abyssal plain sediments characterized by rock-magnetic and geochemical indices. Mar. Geol. 163 (1), 77–107.
Rowan, C.J., Roberts, A.P., Broadbent, T., 2009. Reductive diagenesis, magnetite dissolution, greigite growth and paleomagnetic smoothing in marine sediments: a new view. Earth Planet. Sci. Lett. 277 (1–2), 223–235.
Schimmelmann, A., 2011. The "coffin lid" effect: flood layers and turbidites in Santa Barbara Basin affect diagenesis of organic matter in underlying varved sediment. In: Besonen, M.R. (Ed.), Second Workshop of the PAGES Varves Working Group. Corpus Christi, Texas, USA, pp. 83–86.
Schimmelmann, A., Kastner, M., 1993. Evolutionary changes over the last 1000 years of reduced sulfur phases and organic carbon in varved sediments of the Santa Barbara Basin, California. Geochim. Cosmochim. Acta 57, 67–78.
Schimmelmann, A., Lange, C.B., Berger, W.H., 1990. Climatically controlled marker layers in Santa Barbara Basin sediments and fine-scale core-to-core correlation. Limnol. Oceanogr. 35 (1), 165–173.
Schimmelmann, A., et al., 1992. Extreme climatic conditions recorded in Santa Barbara Basin laminated sediments: the 1835–1840 Macoma event. Mar. Geol. 106 (1992), 279–299.
Scholz, F., McManus, J., Mix, A.C., Hensen, C., Schneider, R.R., 2014. The impact of ocean deoxygenation on iron release from continental margin sediments. Nat. Geosci. 7 (6), 433–437.
Schwertmann, U., 2008. Iron oxides. In: Chesworth, W. (Ed.), Encyclopedia of Soil Science. Springer, Dordrecht, pp. 353–369.
Scott, C., et al., 2008. Tracing the stepwise oxygenation of the Proterozoic Ocean. Nature 452 (7186), 456–459.
Severmann, S., Lyons, T.W., Anbar, A.D., MacManus, J., Gordon, G.W., 2008. Modern iron isotope perspective on the benthic iron shuttle and the redox evolution of ancient oceans. Geology 36 (6), 487–490.
Shiller, A.M., Gieskes, J.M., Brian Price, N., 1985. Particulate iron and manganese in the Santa Barbara Basin, California. Geochim. Cosmochim. Acta 49 (5), 1239–1249.
Smirnov, A.V., Tarduno, J.A., 2000. Low-temperature magnetic properties of pelagic sediments (Ocean Drilling Program Site 805C): tracers of maghemitization and magnetic mineral reduction. J. Geophys. Res. 105 (B7), 16457–16471.
Soutar, A., Crill, P.A., 1977. Sedimentation and climatic patterns in the Santa Barbara Basin during the 19th and 20th centuries. Geol. Soc. Am. Bull. 88 (8), 1161–1172.
Stolz, J.F., Chang, S.-B.R., Kirschvink, J.L., 1986. Magnetotactic bacteria and single-domain magnetite in hemipelagic sediments. Nature 321, 849–851.
Tessin, A., Sheldon, N.D., Hendy, I., Chappaz, A., 2016. Iron limitation in the Western Interior Seaway during the Late Cretaceous OAE3 and its role in phosphorus recycling and enhanced organic matter preservation. Earth Planet. Sci. Lett. 449 (2016), 135–144.
Tribovillard, N., Algeo, T.J., Lyons, T., Riboulleau, A., 2006. Trace metals as paleoredox and paleoproductivity proxies: an update. Chem. Geol. 232 (1–2), 12–32.
Tribovillard, N., Algeo, T.J., Baudin, F., Riboulleau, A., 2012. Analysis of marine environmental conditions based onmolybdenum–uranium covariation—applications to Mesozoic paleoceanography. Chem. Geol. 324-325, 46–58.
Vorlicek, T.P., Kahn, M.D., Kasuya, Y., Helz, G.R., 2004. Capture of molybdenum in pyrite-forming sediments: role of ligand-induced reduction by polysulfides. Geochim. Cosmochim. Acta 68 (3), 547–556.
Vorlicek, T.P., Chappaz, A., Groskreutz, L.M., Young, N., Lyons, T.W., 2015. A new analytical approach to determining Mo and Re speciation in sulfidic waters. Chem. Geol. 403, 52–57.
Wang, Y., Hendy, I., Napier, T.J., 2017. Climate and anthropogenic controls of coastal deoxygenation on interannual to centennial timescales. Geophys. Res. Lett. 44 (22), 11528–11536.
Warrick, J.A., Farnsworth, K.L., 2009a. Dispersal of river sediment in the Southern California Bight. vol. 454. pp. 53–67.
Warrick, J.A., Farnsworth, K.L., 2009b. Sources of sediment to the coastal waters of the Southern California Bight. Geol. Soc. Am. Spec. Pap. 454, 39–52.
Wijsman, J.W.M., Middelburg, J.J., Heip, C.H.R., 2001. Reactive iron in Black Sea sediments: implications for iron cycling. Mar. Geol. 172 (2001), 167–180.
Yücel, M., Luther, G.W., Moore, W.S., 2010. Earthquake-induced turbidite deposition as a previously unrecognized sink for hydrogen sulfide in the Black Sea sediments. Mar. Chem. 121 (1–4), 176–186.
van der Zee, C., Roberts, D.R., Rancourt, D.G., Slomp, C.P., 2003. Nanogoethite is the dominant reactive oxyhydroxide phase in lake and marine sediments. Geology 31 (11), 993–996.
Zheng, Y., Anderson, R.F., Geen, A.V., James, K., 2000. Authigenic molybdenum formation in marine sediments: a link to pore water sulfide in the Santa Barbara Basin. Geochim. Cosmochim. Acta 64 (24), 4165–4178.